Materials and Design 166 (2019) 107615

Contents lists available at ScienceDirect

Materials and Design

journal homepage: www.elsevier.com/locate/matdes

Damage progression in thermal barrier coating systems during thermal cycling: A nano-mechanical assessment

Giovanni Bolelli [a,*], Maria Grazia Righi [a], Muhammad Zeeshan Mughal [b], Riccardo Moscatelli [b], Omar Ligabue [c], Nelso Antolotti [c], Marco Sebastiani [b], Luca Lusvarghi [a], Edoardo Bemporad [b]

[a] Department of Engineering "Enzo Ferrari", University of Modena and Reggio Emilia, Via Pietro Vivarelli 10/1, I-41125 Modena, MO, Italy
[b] Roma Tre University, Engineering Department, Via della Vasca Navale 79, 00146 Rome, Italy
[c] Turbocoating S.p.A., via Mistrali 7, I-43043 Rubbiano di Solignano, PR, Italy

HIGHLIGHTS

- Nanomechanical properties of thermal barrier coatings were measured by high-speed nanoindentation and pillar splitting
- During thermal cycling, delamination damage progresses slowly as long as the bond coat forms a dense, tough oxide scale
- The fracture toughness of the thermally grown oxide scale drops when its thickness exceeds a 5-μm threshold
- Severe delamination damage starts from the embrittled thermally grown oxide and propagates across the zirconia top coat
- Such propagation is favoured by a simultaneous drop in top coat strength, due to accumulated microstructural alterations

GRAPHICAL ABSTRACT

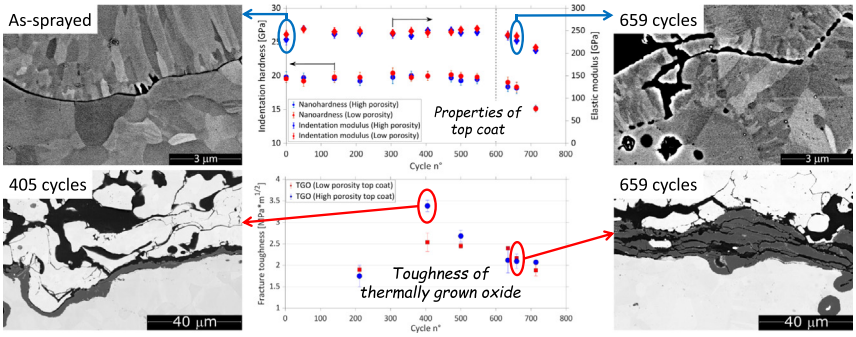

ARTICLE INFO

Article history:
Received 31 October 2018
Received in revised form 14 January 2019
Accepted 18 January 2019
Available online 23 January 2019

Keywords:
Thermal barrier coating
Fracture toughness
Nanohardness
High-speed nanoindentation
Thermal cycling fatigue

ABSTRACT

This paper studies how the nano-mechanical properties of thermal barrier coatings (TBCs) vary during thermal cycling, as a way to shed new light on their failure mechanisms. In particular, high-throughput nanoindentation revealed the evolution of hardness and elastic modulus distributions of plasma-sprayed yttria-stabilized zirconia (YSZ) top layers. The evolution of fracture toughness of the YSZ layers and the thermally grown oxide (TGO) formed onto the vacuum plasma-sprayed NiCoCrAlY bond coat were investigated by nanoindentation micro-pillar splitting. The TGO fracture toughness increases up to ≈2.5–3.5 MPa√m at the early stages of thermal cycling, followed by a rapid decrease to ≈2.0 MPa√m after a critical TGO thickness of ≈5 μm is reached. Consequently, interface damage is initially limited to short cracks within the YSZ material. As TGO thickness exceeds the critical threshold, multiple cracks originate within the TGO and join through the YSZ to form long delamination cracks. Joining is favoured by a simultaneous loss in YSZ strength, testified by a decrease in the nanomechanical properties (hardness, elastic modulus) of both high- and low-porosity top coats. This is due to microstructural changes occurring because of the continuous interplay between sintering and thermal shock cracking in the YSZ layers.

* Corresponding author.
E-mail address: giovanni.bolelli@unimore.it (G. Bolelli).

https://doi.org/10.1016/j.matdes.2019.107615

1. Introduction

Thermal barrier coatings (TBCs) are an important element of modern gas turbines, as they provide thermal insulation and oxidation/hot corrosion protection to hot-section components (e.g. blades, vanes, combustion liners and transition ducts) [1–4]. They usually consist of an oxidation resistant, metallic bond coat, such as an MCrAlY (M = Ni and/or Co) overlay or a Pt-Al diffusion layer, and a thermally insulating, porous ceramic top coat, normally obtained by electron-beam physical vapour deposition (EB-PVD) in aero-engine applications or by atmospheric plasma spraying for land-based gas turbines [1–4]. In either case, the material of choice for the top coat has long been and, in many cases, still is ZrO_2 stabilized with 7–8 wt% Y_2O_3 (yttria-partially stabilized zirconia – YSZ) [5]. Apart from having a rather high thermal expansion coefficient [2] of ≈10–11 × 10^{-6} $°C^{-1}$ [1,4], better matched to that of Ni-based superalloy substrates in comparison to many other refractory oxides, it is also relatively stable under thermal cycling conditions. When manufactured through a rapid cooling process, YSZ indeed develops a non-transformable tetragonal phase (denoted as *t′*) [6]. Due to its peculiar ferroelastic behaviour, this phase exhibits particularly high toughness: its energy release rate $\Gamma = 45 \pm 5$ J/m^2 is, for instance, much higher than that of a cubic ZrO_2–20 wt% Y_2O_3 compound ($\Gamma = 6 \pm 2$ J/m^2) [7]. Although the *t′*-phase is thermodynamically metastable, its transformation kinetics back to the equilibrium mix of cubic (*c*) and tetragonal (*t*) structures is very slow under isothermal or cyclic conditions at temperatures up to at least 1200 °C [6], allowing for a long service lifetime.

Since ever-increasing combustion temperatures are desirable to enhance the thermodynamic efficiency of gas turbines, the functional importance of thermal barrier coatings has been growing. They start becoming prime-reliant constituents [8,9], i.e. they are an integral part of the component design and are needed in order to ensure its proper functionality (at least, its reparability after the designed service time [9]). The main hindrance against achieving the statistical reliability required for prime reliance [9] is the tendency of the ceramic top layer to suffer damage through various mechanisms, e.g. cracking and spallation during thermal cycling, erosion by foreign particles' impingement, hot corrosion by molten salts or chemical attack by molten silicate deposits, etc. [2,10,11].

Cracking and spallation during thermal cycling is a particularly critical phenomenon [4], which has multiple potential causes:

(1) Porous YSZ becomes stiffer and less compliant because of sintering at a high temperature; therefore, thermal shock during cooling can cause transverse cracking across the layer [11–13];
(2) The *t′* phase is progressively de-stabilized at high temperature, through a rather complex transformation process, investigated in great detail in the literature. At first, a modulated texture of coherent yttria-rich and yttria-lean domains is formed within the original *t′* grains [14,15]. This structure still appears as a single *t′* phase (pseudo-*t′* [14]) in a conventional XRD pattern, due to coherency strains between the two domains. For longer exposure times at high temperatures, the coherent structure unravels: if the original *t′* grain is large, the domains coarsen progressively and lose coherence; if the grain is fine, a yttria-rich phase nucleates and grows along the boundary, and can also drain yttria out of adjacent grains [6,15,16]. In either case, the result is the formation of a yttria-rich *c* phase (which turns into a yttria-rich *t″* tetragonal phase when cooled at low temperature) and a yttria-poor *t* phase [6,15,16]. When the grain size of the latter is sufficiently coarse, it readily transforms into monoclinic (*m*) phase during cooling. The ≈4% volume change associated with this transformation induces undesirable stresses in the system [2,9];
(3) Thermal expansion mismatch stresses arise in the interface region between the bond coat and top coat. The alumina-based thermally grown oxide (TGO) scale developed on the bond coat significantly worsens this situation, due to its stiffness and its lower thermal expansion coefficient compared to the YSZ top coat. Large stresses, therefore, result in the formation and propagation of delamination cracks, proceeding through different mechanisms for EB-PVD YSZ layers deposited onto a smooth surface and for plasma-sprayed YSZ deposited onto a rough bond coat surface [4,11,17].

Focussing on plasma-sprayed YSZ layers [4,18,19], cracks can (i) develop on top of the roughness crests (at the TGO/YSZ or TGO/bond coat interface, or within the TGO) and then propagate into the YSZ top coat, usually at off-peak locations where maximum tensile normal stresses are found [20,21]; (ii) develop directly into the YSZ top coat, at the off-peak position between roughness asperities, and propagate towards the TGO; (iii) propagate in the top coat through opening of pre-existing microcracks above the interface [4,18]. Crack growth is particularly accelerated once the TGO grows beyond a "critical thickness" threshold [22]: very large out-of-plane tensile stresses at roughness peaks [21] indeed favour mechanism (i). Horizontal cracks, therefore, become longer [18] and join into a large delamination crack going from one roughness peak to the other along the YSZ layer [22].

The references cited above show that these mechanisms have been investigated in detail through structural and microstructural analyses and finite element simulations; however, little or no information is available on how the micromechanical properties of the constituents (notably, the YSZ top coat and the TGO) change during such transformations. Knowledge of the micromechanical characteristics of the constituents could help to shed further light onto the observed mechanisms, justifying for instance why a thicker TGO becomes particularly prone to cracking, or showing whether the intrinsic properties of YSZ change as a function of possible structural evolutions at high temperature.

Such study has been hindered, up to now, by the considerable experimental difficulty to probe the characteristics of such small volumes of a highly heterogeneous material; however, some recently introduced techniques can offer novel opportunities in this sense: high-speed nanoindentation and pillar-splitting techniques.

High-speed (or high-throughput) nanoindentation represents an innovative approach for the nanomechanical characterization of single and multi-phase materials [23–25]. The method is based on the same principles of the standard instrumented nanoindentation and the Oliver-Pharr analysis [26,27], but, thanks to specific improvements in the measurement hardware, electronics, and data management, it allows to realize a very large number of tests in a very short time (from 1 to 5 s for a complete load-unload sequence). The final output of a high-speed test is therefore represented by a very wide matrix of data points (hardness and indentation modulus), thus enabling robust statistical analysis using standard cumulative deconvolution techniques. One of its most significant applications is to map the mechanical properties of heterogeneous materials [28,29], which is particularly useful for the characterization of TBC systems.

Pillar splitting is a simple method that relies on the sharp nanoindentation of micro-pillars milled in the material through a focused ion beam (FIB). Fracture toughness is easily calculated through eq. (1) by only measuring the indentation load needed to split the pillar, the pillar radius and hardness/modulus ratio of the material [30,31]:

$$K_c = \gamma \frac{P_c}{R^{3/2}} \quad (1)$$

where K_c is the fracture toughness (MPa·m$^{1/2}$), P_c is the critical load for pillar splitting (mN), R is the pillar radius (μm) and γ is a dimensionless coefficient, calculated by Finite Element Modelling (FEM) for a wide range of material properties and indenter geometries in recent papers [31,32]. It is worth noting that the γ coefficient contains the influences of elastic and plastic properties and is consequently material-specific. The expression was originally developed for a Berkovich indenter with

a fixed Poisson's ratio of 0.25; however, the applicability of the technique has been further extended to accommodate different indenter geometries with angles ranging from 35.3^0 (cube-corner) to 65.3^0 (Berkovich) [32].

A significant advantage of this approach is that the measurement of crack length is not required, and there is no effect of residual stresses, which are released as the pillar is separated by the surrounding material during the FIB milling process [33]. Furthermore, there is reduced effect of FIB damage on fracture toughness measurement, in comparison with other micro-scale methods [34], as the crack initiation and growth occur entirely from the core of the pillar which is least affected by the FIB process [34]. The applicability of the method has been demonstrated for a wide range of materials; such as bulk silicon [30], thin ceramic films (TiN, CrN) [30,35], composite coatings ($CrAlN/Si_3N_4$) [31] and heterogeneous ceramic materials like $Li_xMn_2O_4$ battery cathode [36,37].

Focusing on the most critical elements of the TBC system, i.e. the YSZ top coat and the TGO layer, the purpose of this paper is therefore to describe the evolution of their micromechanical properties during thermal cycling fatigue (TCF), tested under service-relevant conditions. Hardness and elastic modulus of the YSZ top coat, mapped through high-speed nanoindentation, and fracture toughness of both the top coat and the TGO, obtained through the pillar-splitting technique, are measured and their trends are discussed in the light of the microstructural evolution and damage progression in the TBC system.

2. Experimental methods

2.1. Coating manufacturing and thermal cycling tests

TBC samples consist of a NiCoCrAlY bond coat (Co 23%, Cr 17%, Al 12.5%, Y 0.45%, Ni bal., values in wt%) deposited by High Velocity Oxygen-Fuel (HVOF) spraying and an atmospheric plasma-sprayed 93 wt% ZrO_2 + 7 wt% Y_2O_3 (YSZ) top coat. Coatings were deposited onto Hastelloy-X disks of 25.4 mm diameter × 3 mm thickness at an industrial manufacturing facility. Two different sets of standard plasma spraying conditions, normally employed to coat diverse components of land-based industrial gas turbines (IGTs), were employed in order to deposit a high-porosity and a low-porosity top coat, which can be considered as representative of the current state of the art. Following conventional procedures, all samples were subjected to a vacuum heat treatment at 1100 °C for 1 h, in order to harden the superalloy substrate, promote metallurgical bonding with the NiCoCrAlY layer, and precipitate the β-NiAl phase within the latter.

Multiple samples were subjected to a thermal cycling test designed to mimic the actual TCF conditions experienced by IGT components. Tests were carried out using a lift furnace and involved rapid (>150 °C/min) heating to 1100 °C, 50 min isothermal holding, and air jet cooling for 10 min, down to 150 °C, after which, a new heating cycle began. Each sample was extracted after a different numbers of cycles (50, 138, 211, 305, 358, 405, 472, 500, 546, 634, 659, 714) in order to check the evolution of the properties.

2.2. Structural and microstructural characterization

The phase composition of all samples, both in as-deposited conditions and after the various TCF test cycles, was assessed by X-ray diffraction (XRD: X'Pert PRO diffractometer, PANAlytical, Almelo, NL), using Ni-filtered Cu-Kα radiation generated from a conventional tube operated at 40 mA filament current and 40 kV acceleration voltage. Patterns were acquired over the $26° < 2\theta < 80°$ range with a step size of 0.017° and 134 s/step counting time, using a 1D array of solid-state detectors (X'Celerator, PANAlytical).

Using the HighScorePlus software (PANAlytical), patterns were fitted with pseudo-Voigt peak functions and polynomial background. The volume fraction of the m phase (V_m) was obtained from the ratio X_m between the integrated intensities of the $(11\bar{1})$ and (111) peaks of the m phase itself, occurring at $2\theta \approx 28.2°$ and $2\theta \approx 31.5°$ (respectively), and of the main (101) peak of the t' phase at $2\theta \approx 30.2°$, according to Eqs. (2) and (3) [6]:

$$X_m = \frac{I_{m(111)} + I_{m(11\bar{1})}}{I_{m(111)} + I_{m(11\bar{1})} + I_{t(101)}} \tag{2}$$

$$V_m = \frac{P{\cdot}X_m}{1 + (P-1)X_m} \tag{3}$$

where $P \approx 1.3$ is an experimentally determined correction coefficient [6].

The tetragonality of the t' phase, defined as $c/(\sqrt{2}a)$ where c and a are the parameters of the tetragonal lattice, was obtained from the fitted positions of the (004) and (220) peaks, located around $2\theta \approx 74°$ [38].

Phase composition on the sample surfaces was further investigated by micro-Raman spectroscopy (LabRam spectrometer, Horiba Jobin-Yvon, Longjumeau, FR), using a 632.81 nm-wavelength ("red") laser focused through a 100× objective. Five spectra were acquired at random locations onto each as-deposited and thermally cycled sample.

The microstructure of the samples was characterized using a field emission gun-scanning electron microscope (FEG-SEM: Nova NanoSEM 450, FEI, Eindhoven, NL) equipped with an energy-dispersive X-ray (EDX) detector for qualitative and semi-quantitative chemical analysis. Samples were vacuum-mounted in room temperature-setting epoxy resin to avoid pull-out damage, and subsequently cut using a semi-automatic metallographic saw, ground and polished with SiC abrasive papers (down to P2500 size), 3 μm polycrystalline diamond slurry and colloidal silica suspension. Polished samples were ultrasonically cleaned in acetone before observation.

The thickness of the TGO scale developed on top of the bond coat in the thermally cycled samples was measured by image analysis (ImageJ software, NIH, Bethesda, MA, USA) using ten 4000× FEG-SEM micrographs acquired in backscattered electrons (BSE) contrast mode.

Porosity of thermally cycled top coats was measured on polished cross-sections by image analysis (Leica Application Suite software), using three 100× optical micrographs each covering a field of view of 1.36 mm.

2.3. High-speed nanoindentation testing

High-speed nanoindentation was employed to measure the mechanical properties (hardness and elastic modulus) of YSZ top coats. Samples were prepared by vacuum-mounting, cutting and grinding/polishing as described above. Measurements were performed using the iNano nanoindenter (KLA Tencor-Nanomechanics, Oak Ridge, TN, USA), equipped with a standard Berkovich tip, employing the innovative "NanoBlitz3D" procedure. Five matrixes of 25 × 25 indentations were realized over a 50 × 50 μm^2 area on each sample, obtaining a total of 3125 indentations for each specimen. Tests are performed with a prescribed load of 3 mN (selected after the first campaign of standard nanoindentations to evaluate the mean depth obtained with this load and the consequent spacing between two contiguous measurements). For these experiments, the full load-unload cycle is completed in about 1 s. The Poisson's ratio of YSZ and the TGO material were assumed to be 0.25, according to literature [39].

Statistical deconvolution is then adopted to evaluate the properties of the different mechanical phases in the material. The cumulative distribution of each indentation hardness and elastic modulus data set was fitted with a Cumulative Distribution Function (CDF) defined as the sum of several, individual Gaussian cumulative distributions. Each distribution was assumed to represent a "mechanical phase". The number of "mechanical phases" that are present in the material is initially unknown and is determined by the deconvolution process after automated iterative optimisation. Full details on the statistical

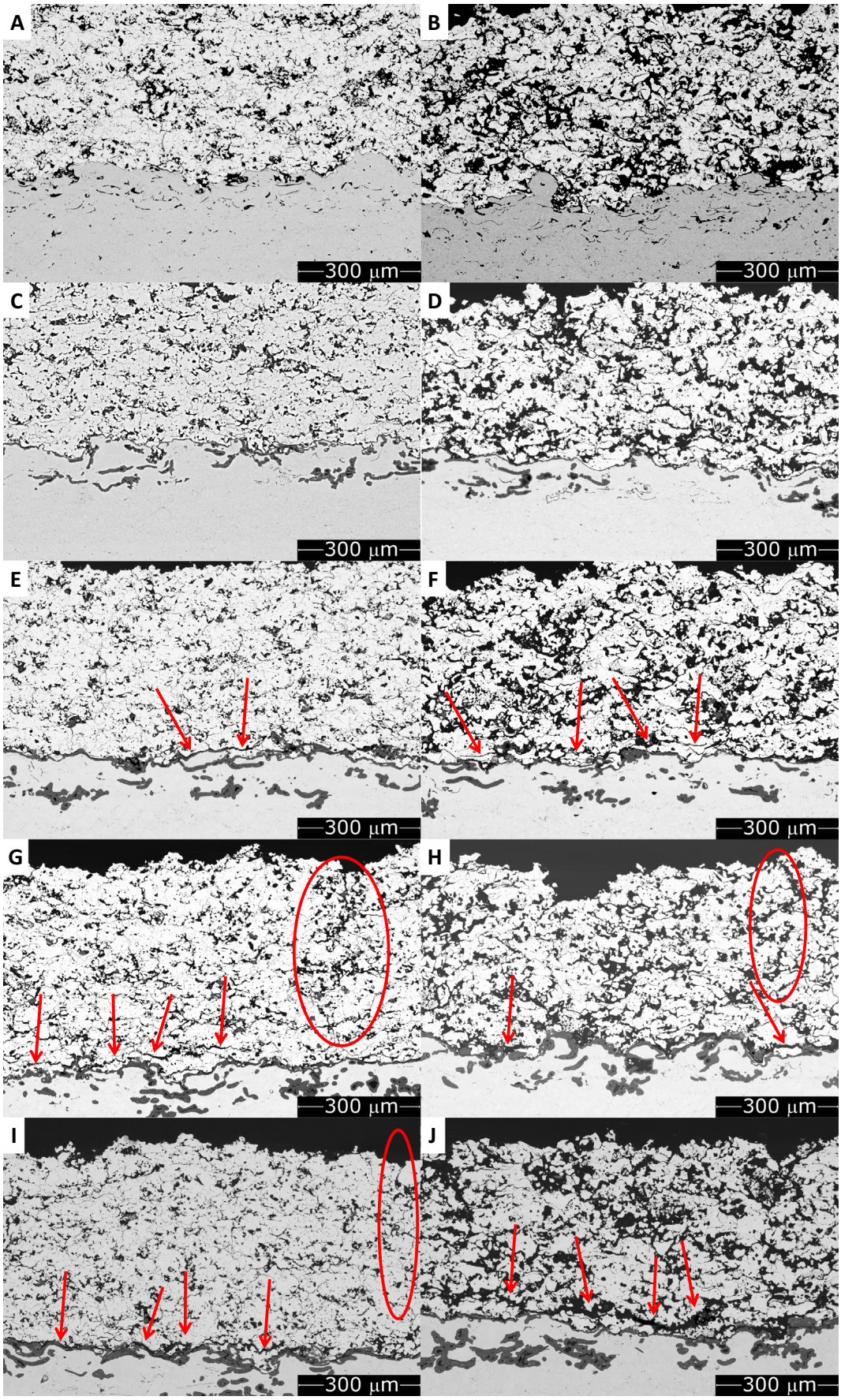

Fig. 1. BSE-SEM overviews of low-porosity (A,C,E,G,I) and high-porosity (B,D,F,H,J) TBC samples, in as-deposited condition (A,B) and after 211 (C,D), 500 (E,F), 634 (G,H) and 714 (I,J) TCF cycles. Circles and arrows indicate transverse and delamination cracks, respectively.

deconvolution procedure are reported in previous papers [23–25]. It is worth noting that some of the mechanical phases could correspond to indentations falling at the interface between two adjacent, microstructurally distinct regions; hence, not all the "mechanical phases" might be significant, as discussed later in the text.

2.4. Micro-pillar splitting tests

Pillars were milled in both the YSZ top coat and the TGO using a focused ion beam in a dual-beam system, equipped with both an SEM column and a FIB column emitting a focused beam of Ga^+ ions (Helios Nanolab 600, FEI). Adopting a procedure that is well described in the earlier papers where pillar splitting was first introduced [30,31], pillars were coarsely milled at 0.92 nA current and finely milled at 48 pA, in order to minimise FIB artefacts. The ion beam voltage was 30 kV. The strategy for FIB milling consisted of a single outer-to-inner pass of the ion beam to create the pillar. The mentioned studies have demonstrated that this is the optimal procedure for minimising FIB artefacts and obtaining a perfectly straight pillar.

Pillar diameters of 4.5 μm and 3.5 μm were selected for the YSZ top coat (where pillars are milled inside splats) and the TGO, respectively. This ensures high spatial resolution and reduced FIB-induced damage effects at the same time. At least 5 pillars were milled to an aspect ratio (h/d) of 1.2, where h is the pillar height and d is the top diameter of the pillar. This ratio provides complete residual stress relaxation on the top surface of the pillar [32]. When testing the TGO layer, milling was only performed on areas wide enough to accommodate the entire pillar volume.

Nanoindentations on the pillars were performed using a Berkovich tip on a Keysight G200 nanoindenter. A constant strain rate of 0.05 s^{-1} along with an indentation depth of 400 nm was selected for all tests. To further enhance the reliability of the tests, instrument frame stiffness and indenter area function were calibrated before and after testing on a certified fused silica sample. As reported in previous papers, the splitting load can be identified by clear and unique pop-in events in the load-displacement curve [30,31].

Finally, fracture toughness was determined using Eq. (1) as laid out in the Introduction. The gamma coefficients for both YZS and TGO materials were determined based on the elastic moduli and hardness values, as measured by nanoindentation on the same materials.

3. Results

3.1. Structure and microstructure evolution after TCF testing

The microstructural difference between the LP and HP coatings is seen from their respective overview micrographs in Fig. 1A, B. TCF tests cause visible sintering of the YSZ top coats, with an overall reduction of porosity in both cases (Fig. 2), although the respective microstructures remain considerably different (Fig. 1C, D). A thin TGO layer, recognizable through its dark grey contrast, is formed on top of the brighter bond coat in the early stages of the test. After ≈500 thermal cycles, sintering of the top coat has proceeded further, resulting not only in a slight, additional reduction of porosity (Fig. 2), but, most of all, in qualitative changes to pore shape (Fig. 1E, F). Small delamination cracks (see arrows) have also developed near the YSZ/TGO interface, propagating from roughness crests or nearby off-peak positions, as widely described in the literature and summarized in the Introduction. For increasingly large numbers of cycles, thermal shocking of a progressively sintered YSZ layer results in the formation of transverse cracks (Fig. 1G, H – circles). As a result, the overall porosity increases slightly (Fig. 2). Delamination cracks (arrows) become longer and propagate both in the TGO (especially on asperity peaks) and in the YSZ, including cracks located above the roughness crests as well, in excellent accordance with the known evolution of TCF failure of plasma-sprayed TBCs as described e.g. in [4,17,40].

For >700 cycles (Fig. 1I, J), most of the interface region is eventually cracked. At this stage, the residual life of the TBC is minimal.

The progression of TCF degradation (sintering; delamination and transverse cracking) in the YSZ top coat is accompanied by microstructural transformations in both the bond coat, the top coat, and the TGO, as illustrated separately in the forthcoming Sections 3.1.1–3.1.3.

3.1.1. Microstructural evolution in the bond coat

The bond coat initially consists of a two-phase microstructure: a β-NiAl phase (characterized by its darker greyscale contrast) is surrounded by a (brighter) γ-Ni alloy matrix (Fig. 3A, B). This is the standard microstructure expected of an MCrAlY alloy after a vacuum heat-treatment [1,41], which restores the thermodynamic equilibrium structure eliminating the possible effects of plastic deformation and melt quenching during HVOF deposition. In addition, tiny oxide inclusions (with black contrast in the BSE micrographs of Fig. 3B) appear to follow the original interparticle boundaries of the as-sprayed coating.

This microstructure evolves through a progressive depletion of the β-NiAl phase (Fig. 3), occurring by Al diffusion both upwards, to support the progressive growth of the TGO [41–43], and downwards, towards the Al-poor superalloy substrate [44–46].

After increasingly large numbers of thermal cycles (Fig. 3C–E), the β-NiAl phase is confined to an ever thinner central region (see arrows). Most of the bond coating is depleted of β-NiAl after 634 cycles (Fig. 3E, F), and the surviving β-NiAl phase displays morphological changes, better seen in the magnified view of Fig. 4. Diffusion processes indeed alter the composition of β-NiAl, resulting in a slight excess of Ni which is also known to cause the formation of lamellae of tetragonal

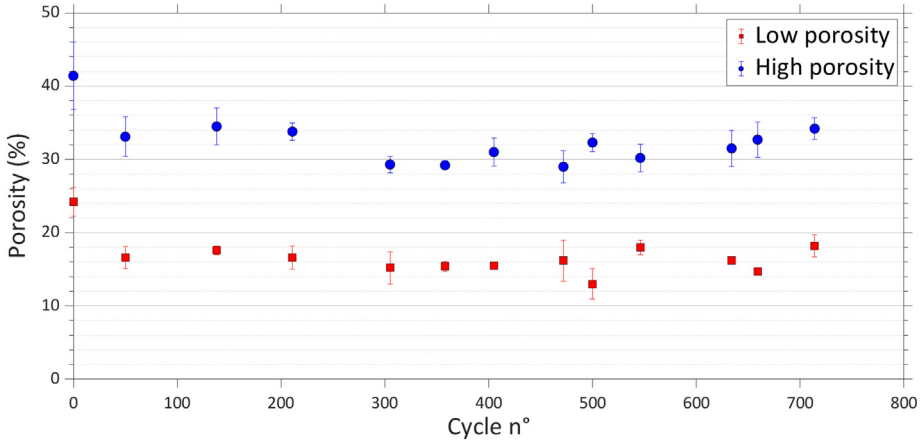

Fig. 2. Evolution of top coat porosity as a function of the number of thermal cycles.

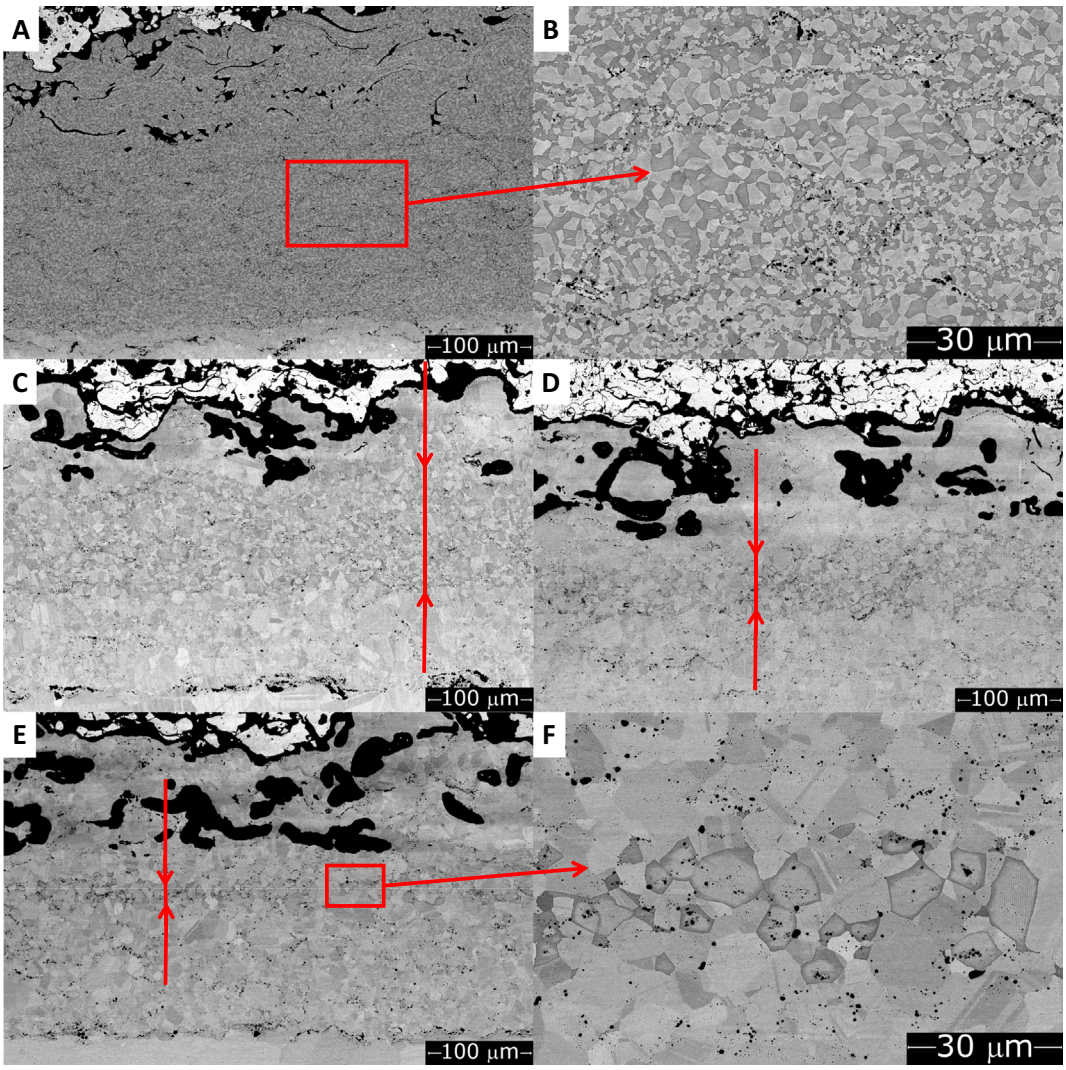

Fig. 3. BSE-SEM micrographs of the bond coat in as-deposited condition (A: overview, B: detail), after 405 (C), 500 (D) and 634 (E: overview, F: detail) TCF cycles. Arrows indicate the residual β-NiAl containing area.

martensite [47–51]. Martensitic lamellae sometimes becomes large enough to be seen through electron channelling contrast in BSE-SEM micrographs (Fig. 4: label 1). At the same time, the surrounding γ-Ni matrix develops large twins (label 2). Almost no β-phase remains after 714 cycles.

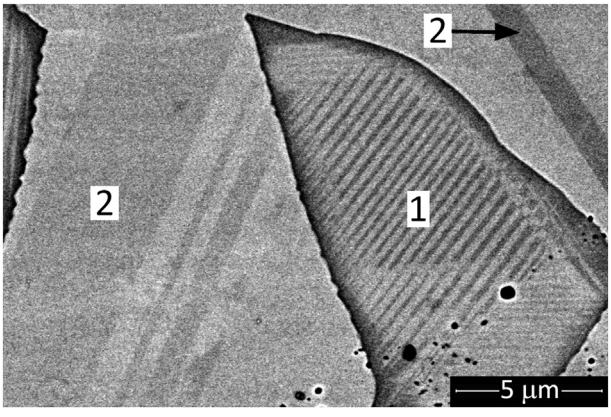

Fig. 4. Magnified BSE-SEM detail of the bond coat after 634 TCF cycles. Label 1 = lamellar martensite in a β-NiAl grain; label 2 = twins in the γ-Ni matrix.

3.1.2. Evolution of the TGO

At the early stages of the TCF test, cyclic exposure of the bond coat to high temperatures results in a thin, dense and compact TGO layer (Fig. 5A), mostly consisting of alumina with tiny yttrium-rich inclusions (Fig. 6A, B) [41].

After ≈400 cycles, the TGO still presents limited thickness and little damage (Fig. 5B), except for prominent roughness crests, where the TGO is somewhat thicker and microcracked (Fig. 5C). After 500 cycles, the thickness has increased slightly more, and, at this point, substantial crack formation starts even on relatively smooth regions (Fig. 5D, E). Moreover, other, more defective oxides appear, sometimes forming remarkably large protrusions as seen in Fig. 5E.

EDX spectra reveal high concentrations of Ni and Co (Fig. 6C, D). It should be reminded that, since a low e-beam acceleration voltage of 8 kV was employed, small amounts of Cr within these protrusions may have gone undetected as the intensity of the Cr-K lines would be too low under these conditions, while the oxygen signal overlaps the Cr-L lines.

Upon further cycling, the TGO thickness starts increasing much more rapidly (Fig. 7A): after ≈650 cycles (Fig. 5F), for instance, the TGO has become considerably thicker and contains even more numerous cracks, which extend to the YSZ layer corresponding to the larger delamination cracks noted in Fig. 1.

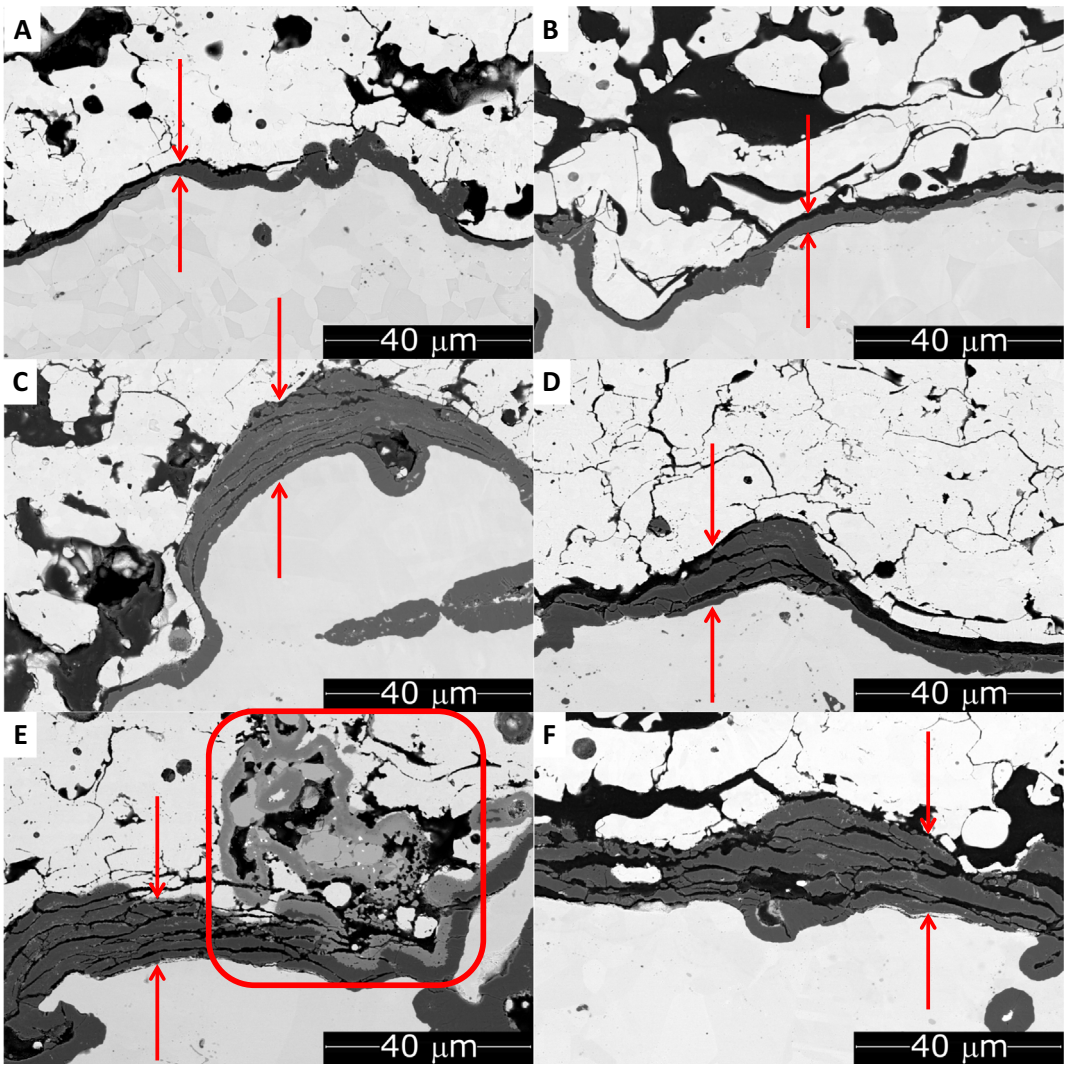

Fig. 5. BSE-SEM micrographs of the TGO layer (marked by arrows) developed onto the bond coat after 138 (A), 405 (B,C), 500 (D,E) and 659 (F) TCF cycles. (Ni,Co)-based oxides are encircled in panel E.

3.1.3. Structural and microstructural evolution of the YSZ top coat

Through the electron channelling contrast in BSE micrographs, the crystal grain morphology in both the high- and low-porosity YSZ top coats can be identified as consisting primarily of equiaxed grains (Fig. 8A: label 1), whose size ranges from sub-micrometric to several micrometres. In addition, some areas with fine columnar grains appear (Fig. 8A: label 2).

Based on their elongated morphology, the latter areas presumably originated from fully molten YSZ particles, which were flattened and impact-quenched onto the underlying surface. Heterogeneous nucleation at the interface and directional solidification during rapid cooling indeed result in a columnar grain structure [52]. Most of the particles making up these porous YSZ coatings were, however, either partially unmelted, thus retaining the original structure of the feedstock powder, or partially re-solidified before impact, which usually results in homogeneous nucleation within the melt during the flight stage. Both occurrences cause the formation of large, poorly-flattened areas with equiaxed grains of various sizes.

This grain morphology is retained through most of the TCF test duration (Fig. 8B, C), in spite of the macroscopically visible sintering noted in Fig. 1 and Fig. 2. Some microstructural alterations, however, appear at later stages of the test, i.e. after ≈550 cycles. On the one hand, columnar grains tend to be re-structured into fine equiaxed grains (Fig. 8D–F: label 3; also compare the magnified views of Fig. 9B and D). On the other hand, very fine, widespread closed porosity appears within the pristine equiaxed-grain areas (Fig. 8D–F). The latter phenomenon is better seen in the details of Fig. 9: compared to the as-deposited coatings (Fig. 9A, B), after many thermal cycles the microcracks are partly healed and turn into closed pores (Fig. 9D: circles). Those pores can become particularly numerous and concentrate in the boundaries between equiaxed grains (Fig. 9C: circle).

In any case, the YSZ top coats seem not to undergo significant structural evolution during the present TCF test. XRD patterns (Fig. 10) show that they consist almost exclusively of the t' phase, with no detectable amount of cubic phase. The amount of monoclinic phase is small (≈2–3%: see Table I) and does not increase during thermal cycling.

Detailed views of the (220) and (004) diffraction peaks of the t' phase highlight a slight increase in tetragonality after the first few cycles, with no subsequent evolution up to the end of the test. The calculated $c/(\sqrt{2}a)$ ratio (Table I) confirms this qualitative observation; it is also noted that the stable tetragonality value of 1.011 is consistent with that of the t' phase as listed in the literature [6,53].

Raman spectra acquired onto the coatings also contain exclusively peaks belonging to the tetragonal phase (Fig. 11), with an evolution (reduction in peak breadth) after the first 50 TCF cycles and no subsequent change for longer testing times (Fig. 11).

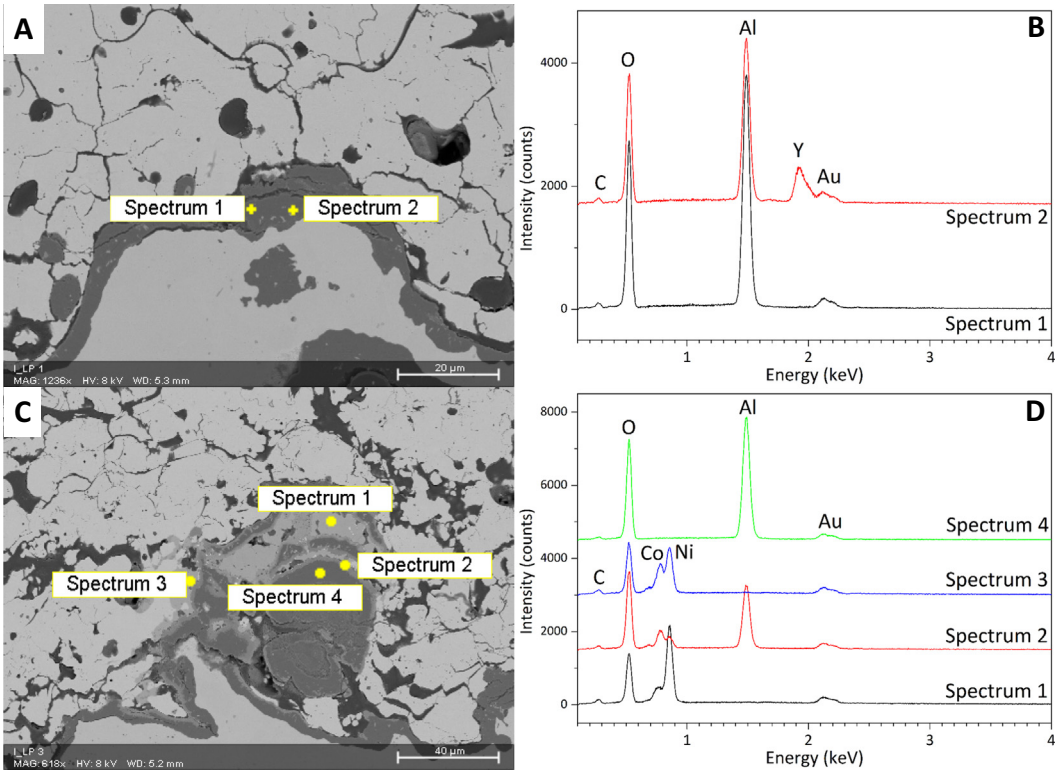

Fig. 6. BSE-SEM micrographs of the TGO layer developed after 500 TCF cycles (A,C) and corresponding EDX spectra acquired at an acceleration voltage of 8 kV (B,D): TGO region consisting of aluminium oxide with yttrium-rich inclusions (A,B) and TGO region with overgrowth of (Ni,Co)-rich oxide protrusions (C,D).

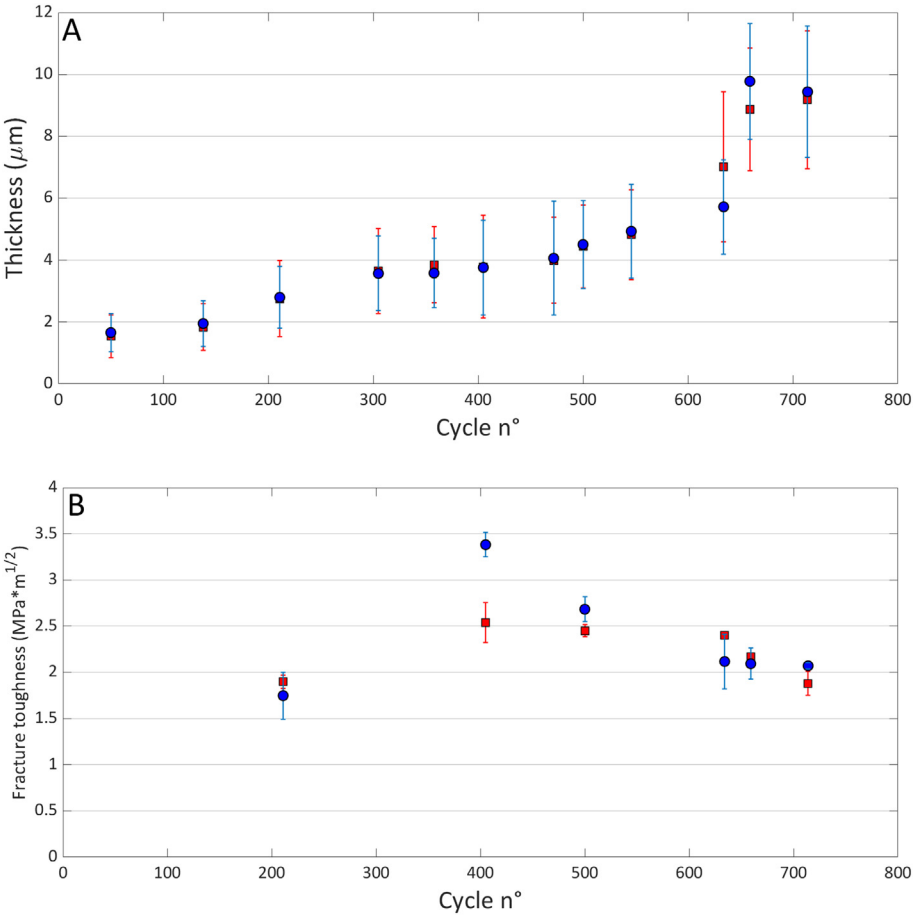

Fig. 7. Evolution of (A) thickness (measured by image analysis) and (B) fracture toughness (by pillar-splitting, Section 3.3.2) of the TGO as a function of the number of TCF test cycles.

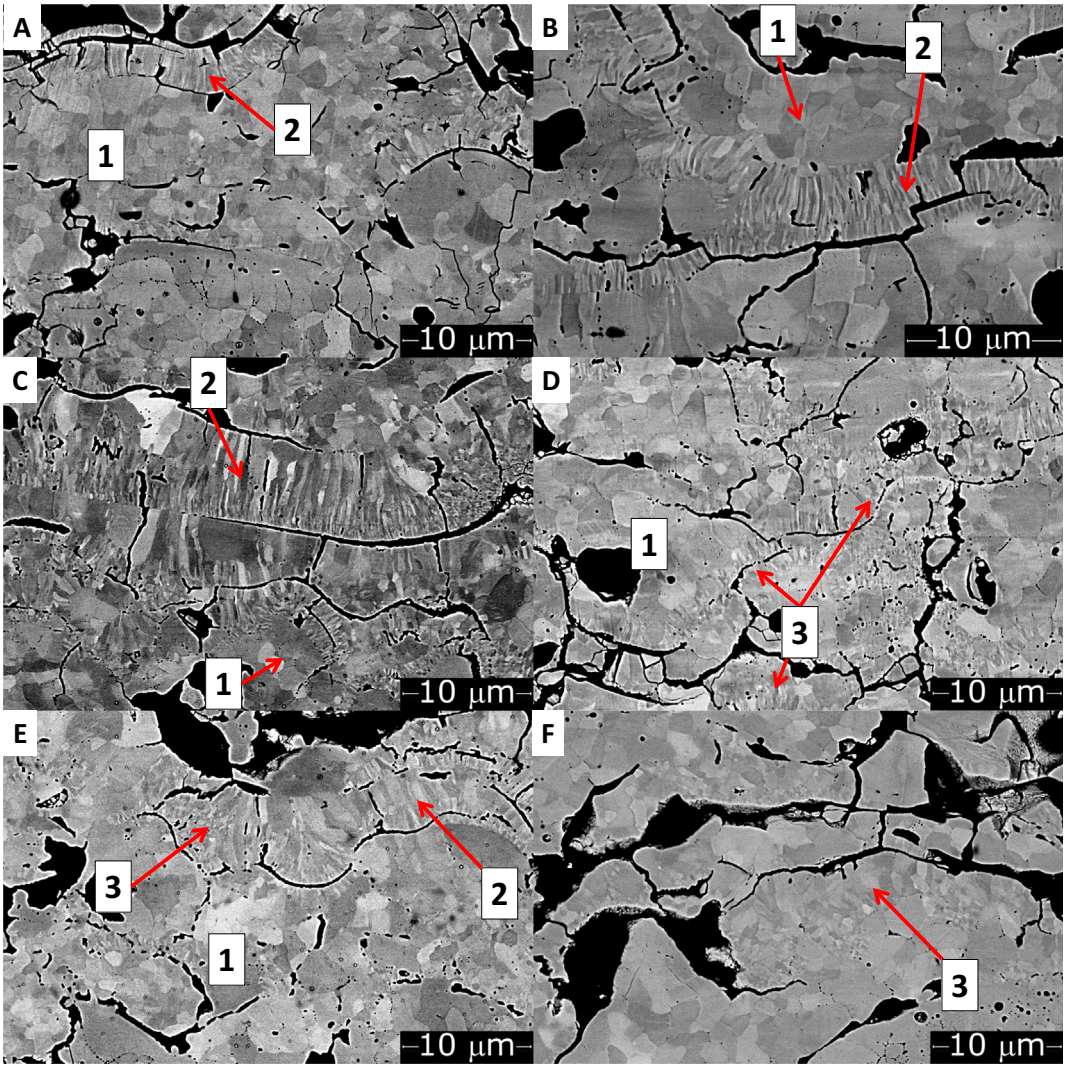

Fig. 8. BSE-SEM micrographs showing magnified views of the cross-section of the low-porosity YSZ coating in as-deposited condition (A) and after 138 (B), 472 (C), 546 (D), 659 (E) and 714 (F) TCF cycles. Label 1 = equiaxed grains area; label 2 = columnar grains area; label 3 = recrystallized columnar grains.

3.2. High-speed nanoindentation of the YSZ top coat

Data distribution plotted in Fig. 12 as hardness vs indentation number (#) shows a mean H_{IT} value of about 15 GPa, but a large number of indentations also returned lower hardness values; hence, data deconvolution, carried out as described in Section 2.3, allowed deeper insight.

In all cases, the best fit could be achieved with three distinct hardness and modulus distributions (often referred to as "mechanical phases", Fig. 13). The first one, related to the lowest values of hardness and elastic modulus, can be ascribed to indentations falling next to or inside the resin-filled porosity; hence, this distribution will not be considered further, as it is not representative of the YSZ material.

SEM observations of the nanoindentation matrixes on the YSZ top coat, such as is presented in Fig. 14, reveal indentations falling on both columnar and equiaxed grains, in addition to some falling in or very close to the resin-filled pores (resulting in the non-significant data making up the first distribution). It is therefore inferred that the second and third mechanical phases can be respectively ascribed to indentations performed on columnar grain regions and equiaxed grain regions of the YSZ top coating. The second mechanical phase accordingly contains a smaller number of data points than does the third, which is consistent with the presence of fewer columnar grain areas within a predominantly equiaxed-grain matrix as observed in Section 3.1.3. This distribution also corresponds to somewhat lower average hardness ($H_{IT} \approx 17$ GPa) and elastic modulus ($E_{IT} \approx 220$ GPa), as compared to the third mechanical phase ($H_{IT} \approx 20$ GPa and $E_{IT} \approx 245$ GPa).

In a previous study, indentation hardness and elastic modulus of plasma-sprayed YSZ coatings were assessed by nanoindentation tests using a prescribed load of 8 mN [54]. The indentation hardness (≈9.9 GPa) and elastic modulus (≈155 GPa) reported in that study are lower than the values obtained in this work for both the columnar and equiaxed grain regions. The prescribed load used here (3 mN) indeed allows probing even smaller volumes, thus reducing the influence from microstructural features such as voids and defects. On the other hand, the chosen load is sufficiently high as to avoid the reverse indentation size effect observed in plasma-sprayed YSZ below 1 mN [55].

The average hardness and modulus values of both the second and the third mechanical phases (Fig. 15) show a clear reduction after ≈600 TCF cycles (marked by a dashed line on the graphs), in both high- and low-porosity coatings.

3.3. Micro-pillar splitting

3.3.1. Fracture toughness of the YSZ top coat

Fig. 16 highlights some representative load-displacement curves of pillars realized within YSZ splats in the top coat. The critical load for pillar splitting can be seen from the displacement burst in the load-

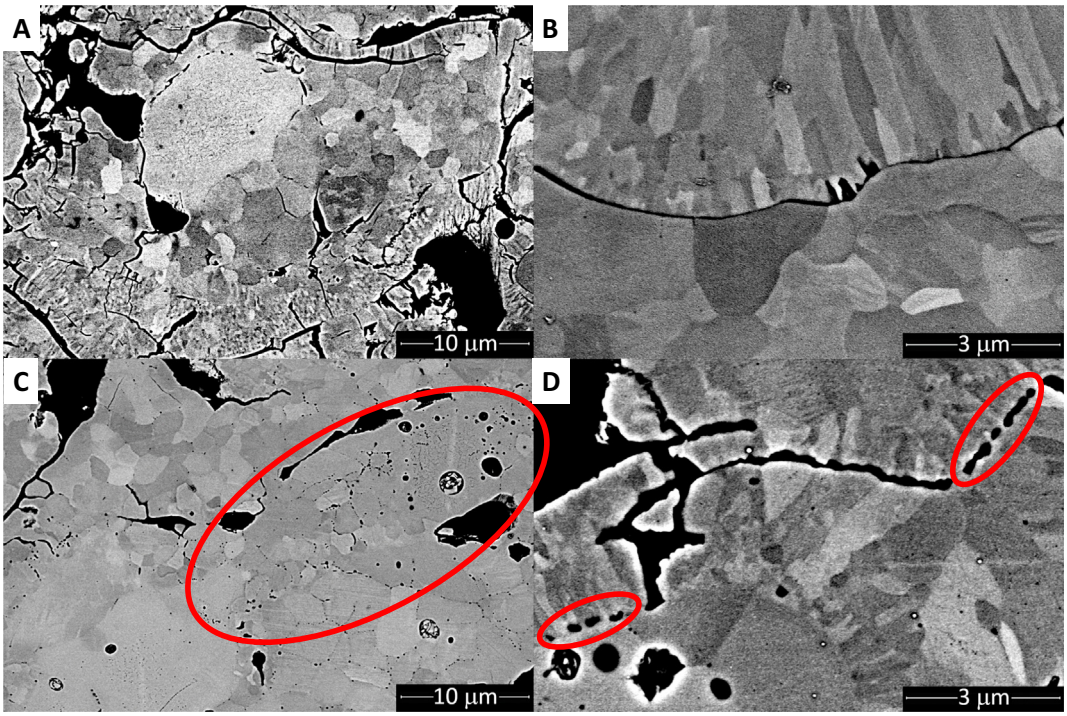

Fig. 9. Comparison between BSE-SEM micrographs of as-deposited and thermally cycled YSZ coatings: low-porosity coating, as deposited (A); high-porosity coating, as-deposited (B); low-porosity coating after 714 cycles (C); high-porosity coating after 659 cycles (D). Circles in panels C, D indicate partially healed microcracks and distributed fine porosity.

displacement curve. After performing a statistically relevant number of experiments, it was observed that splitting load values tend to group at two distinct levels, corresponding to different fracture toughness values according to Eq. (1).

This behaviour could be associated with the different microstructural features within the YSZ coating, as already demonstrated by nanoindentation tests in Section 3.2. This interpretation is validated by associating individual toughness values to the corresponding pillars, imaged by SEM before (Fig. 17) and after splitting (Fig. 18). It is clearly noted that distinct pillars belonging to the same splat produce comparable values of fracture toughness after splitting, consistent with the fact that homogeneous microstructural features are normally encountered within one splat. Remarkably, pillars within the most flattened splat visible in Fig. 17A (which, in accordance with Section 3.1.3, probably consists of columnar grains) return the lowest values.

Looking at some split pillars (Fig. 18), it is noted that those located within a single, large equiaxed grain (Fig. 18) are associated to higher toughness values than are the pillars made in fine-grained areas (Fig. 18B).

It is worth noting that calculation of fracture toughness on single crystal grains might not be an optimal condition, because of the associated uncertainty of crystal orientation and the consequent error in the choice of the elastic constant for the single grain. The calibration of the γ coefficient appearing in Eq. (1) is indeed based on the E/H ratio of the tested material [32]. Without knowing the specific orientation, the homogeneous elastic modulus and hardness values obtained from the nanoindentation experiments were therefore chosen. The resulting E/H value can anyway be considered as a reliable average of the mechanical properties of the samples. In addition, the E/H ratio is surely less sensitive to crystal orientation than is the sole elastic modulus E.

Based on the above considerations, the toughness values of the YSZ top coat are divided and averaged into two distinct groups, hereafter labelled as "region 1" and "region 2", which are respectively assumed to be representative of coarse- and fine-grained regions (including columnar regions). For both coarse-grained "region 1" and fine-grained "region-2", a trend can be observed with respect to the number of thermal cycles (Fig. 19): irrespective of the porosity of the top coat, higher fracture toughness was observed in the as-deposited condition, which decreases and subsequently stabilizes during cycling. In some cases, the decrease is sharper (region 1 in the low-porosity coating), while in others it is minimal (region 2 in the high-porosity coating).

3.3.2. Fracture toughness of the thermally grown oxide (TGO)

The fracture toughness values of the TGO in samples with both high- and low-porosity top coats exhibit similar trends as a function of the number of thermal cycles (Fig. 7B). Note that data points begin at ≈200 cycles because the TGO developed in the earliest stages is too thin to host a FIB-machined pillar. Fracture toughness increases up to ≈400 thermal cycles, where a maximum is observed. With further thermal cycling, fracture toughness decreases, and significantly lower values are observed especially after ≈650 cycles, roughly corresponding to the rapid increase in thickness described in Section 3.1.2 (compare to Fig. 7A).

4. Discussion

Ageing of both high- and low-porosity TBCs during the present TCF tests is the result of processes acting simultaneously in the top coat, the bond coat and the TGO.

In the top coat, no detectable phase change occurs during the entire test duration. According to the ageing severity map plotted in [16], indeed, plasma-sprayed YSZ can survive well above 1000 h at 1100 °C without developing >1% monoclinic phase. The small amount of monoclinic phase present in the coatings is probably due to compositional inhomogeneity of the feedstock powder, i.e. few powder particles might have contained a lower amount of yttria and/or some de-stabilizing impurities.

However, some changes in both the XRD patterns (reflecting a very slight increase in tetragonality: Table I) and Raman spectra were noted in Section 3.1.3. It was argued in [53] that Raman spectra are particularly sensitive to the anion lattice (i.e. to the oxygen atoms lattice); hence, the evolution of the Raman spectra after the first 50 cycles could be ascribed to a re-ordering and reduction of defects in the O^{2-} lattice. Some oxygen vacancies are due to the substitution of Zr^{4+} ions by lower-valence Y^{3+}

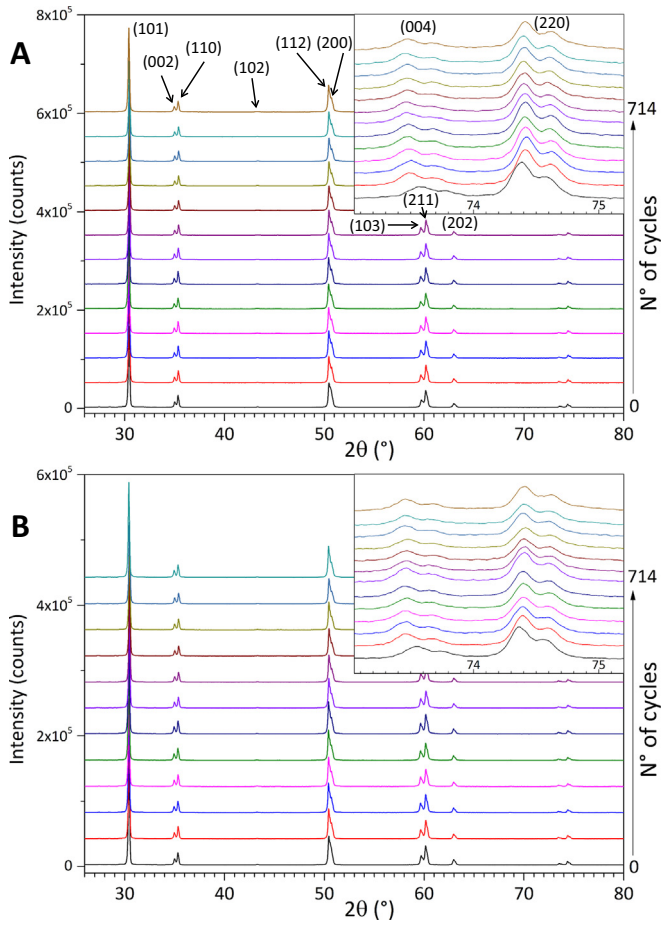

Fig. 10. XRD patterns of the low-porosity (A) and high-porosity (B) YSZ coatings in as-deposited condition and after TCF testing. All peaks are indexed to the t'-ZrO_2 lattice according to JCPDF 48-224. Insets show details of the (004) and (220) peaks around 2θ = 74°.

Table I
Tetragonality of the t' phase and content of monoclinic phase obtained by XRD pattern fitting.

N° of cycles	Type (HP/LP)	m-phase (vol%)	Tetragonality $c/(\sqrt{2}a)$
0	HP	1.7	1.010
	LP	2.8	1.009
50	HP	3.9	1.011
	LP	2.7	1.011
138	HP	3.5	1.011
	LP	2.0	1.011
211	HP	3.0	1.011
	LP	2.7	1.011
305	HP	3.4	1.011
	LP	2.9	1.011
358	HP	2.6	1.011
	LP	3.1	1.011
405	HP	3.1	1.011
	LP	3.7	1.011
472	HP	3.3	1.011
	LP	3.3	1.011
500	HP	3.1	1.011
	LP	3.5	1.011
546	HP	2.8	1.011
	LP	2.1	1.011
634	HP	2.4	1.011
	LP	3.1	1.011
659	HP	2.4	1.011
	LP	1.7	1.011
714	HP	2.6	1.011
	LP	2.7	1.011

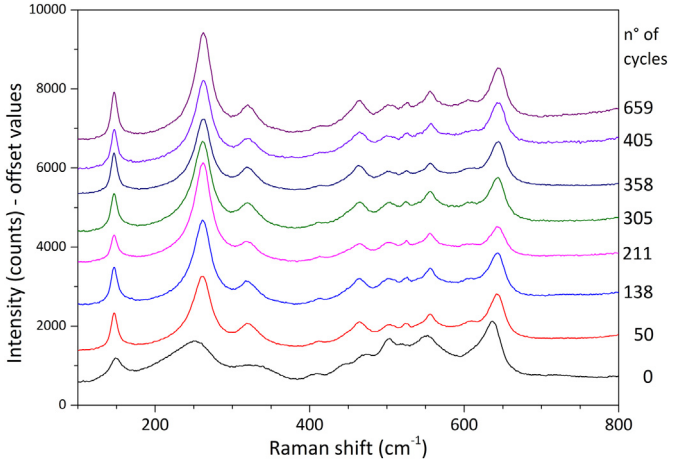

Fig. 11. Evolution of the micro-Raman spectra of the high-porosity YSZ samples during the TCF test.

ions in YSZ [4], but additional loss of oxygen probably occurred during the deposition process, as previously described in [56,57]. Heat treating in the vacuum does not eliminate O^{2-} vacancies. In accordance with [57], it is therefore assumed that those excess vacancies were at least partly recovered during high-temperature holding in the early stages

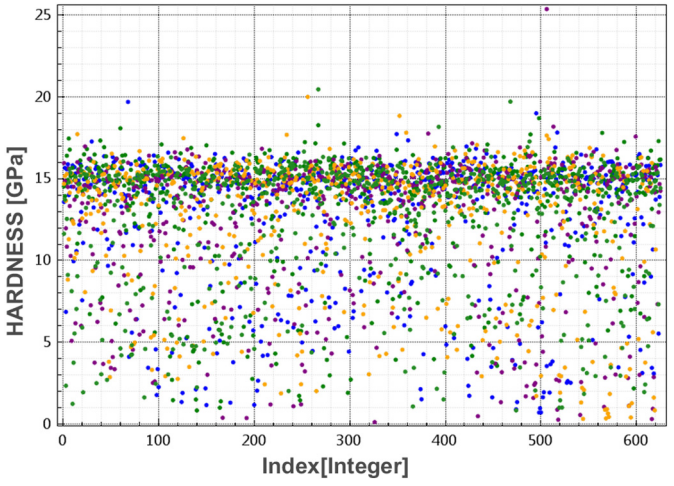

Fig. 12. Indentation hardness (H_{IT}) results from the five 25 × 25 high-speed nanoindentation maps on a low-porosity top coating after 714 thermal cycles. Colours differentiate data from each of the 25 × 25 maps.

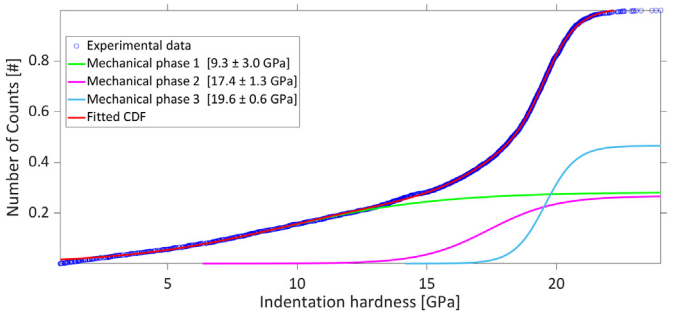

Fig. 13. Statistical deconvolution of indentation hardness (H_{IT}) results from the five 25 × 25 high-speed nanoindentation maps on the high-porosity YSZ top coating after 138 TCF cycles. Mechanical phase 1 = indentation on or next to the resin-filled voids; Mechanical phase 2 = indentations on columnar grain regions; Mechanical phase 3 = indentations on equiaxed grain regions.

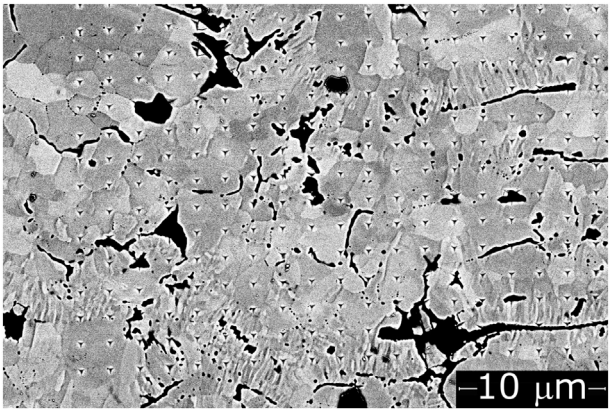

Fig. 14. BSE-SEM micrograph showing part of a nanoindentation matrix on the low-porosity YSZ top coat after 358 TCF cycles.

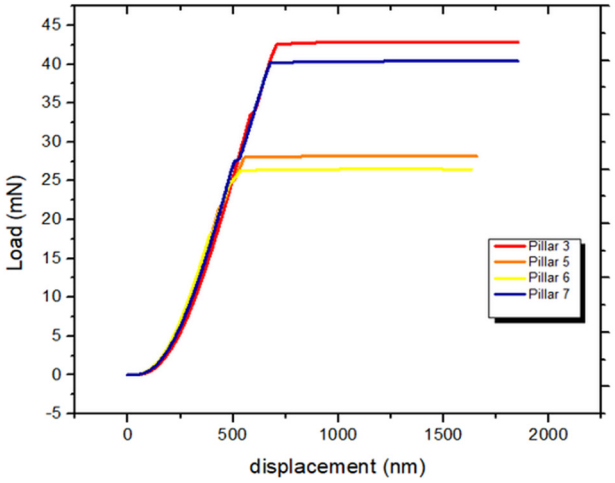

Fig. 16. Load-displacement curves obtained during pillar splitting by a depth-sensing Berkovich nanoindenter on a TBC coating, showing two different pillar splitting loads.

of the TCF test, which explains the observed sharpening of the Raman peaks. Oxygen uptake could have also brought about a very slight expansion of the lattice in the *c* direction, explaining the modest increase in tetragonality.

It is found in the present work that such change, albeit small, is not without consequences for the "intrinsic" mechanical properties of YSZ. A slight but perceivable decrease in fracture toughness is noted in both fine- and coarse-grained areas after the first 50 TCF cycles. The ferroelastic mechanism which underlies the toughness of *t'*-YSZ [7] is indeed critically dependent on its structure so that any re-arrangement can affect it.

Analysing the data in detail, the initial fracture toughness of coarse-grained "region 2" before thermal cycling ($K_{IC} \approx 3.5$ MPa·√m: Fig. 19) corresponds to an energy release rate $\Gamma = K_{IC}^2/[E/(1-\nu^2)] \approx 47$ J/m^2, assuming that YSZ possesses an elastic modulus E ≈ 245 GPa (Fig. 15A) and a Poisson's ratio $\nu = 0.25$ (Section 2.3). This value is in remarkably good agreement with the toughness of bulk *t'*-YSZ ($\Gamma = 45 \pm 5$ J/m^2 [7]). In case of testing over polycrystalline areas ("region 1" in Section 3.3.1), on the other hand, lower toughness results from

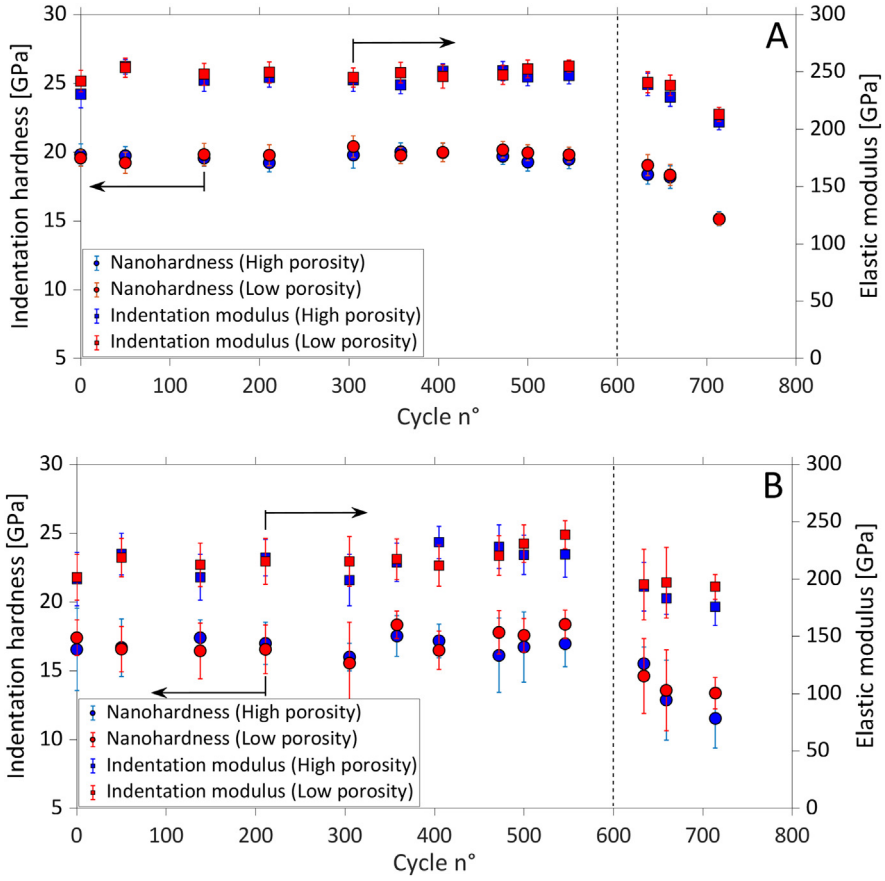

Fig. 15. Evolution of indentation hardness and modulus (mean value ± standard deviation) for the third (A) and second (B) mechanical phases in the HP and LP TBC samples, as a function of the number of thermal cycles.

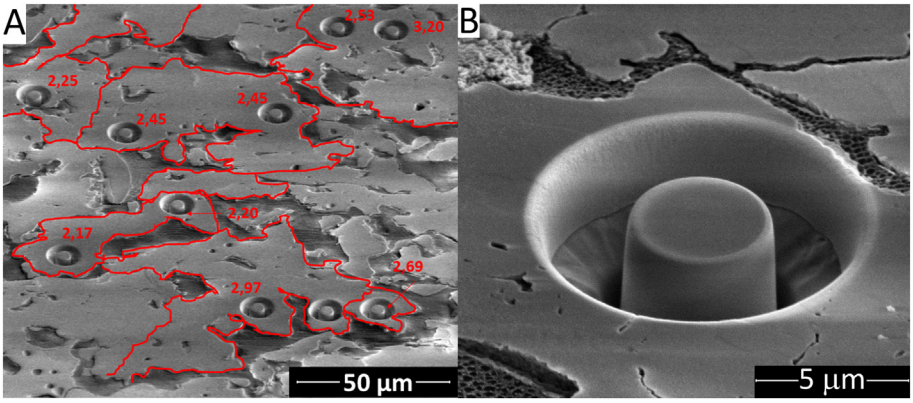

Fig. 17. SEM micrographs of the cross-section of a YSZ coating with milled micro-pillars for fracture toughness measurement: A – overview; B – detail of a pillar. Numbers next to each pillar represent the fracture toughness obtained by subsequent splitting (in MPa·√m). Splat boundaries are highlighted in red.

the presence of multiple grain boundaries inside the pillar volume. Interestingly, a previous study found that having a fine grain size in a plasma-sprayed YSZ coating is undesirable because it worsens the long-term stability of the *t′* phase [15]. In the present work, even though the TCF test conditions were not severe enough to destabilize the *t′* phase, it is additionally found that having a fine grain size is undesirable also because it reduces fracture toughness.

It is possible that, in accordance with the literature summarized in the Introduction, the initial changes to the structure and fracture toughness are also due to re-arrangement of the original *t′* phase into a pseudo-*t′* structure made of coherent yttria-rich and yttria-lean domains [53,58]. However, as noted previously, the test temperatures were not high enough to result in detectable loss of coherency for longer exposure times.

As a result, TCF failure in the present TBC systems reflects almost exclusively stress build-up due to TGO growth (Section 3.1.2) and top coat sintering (Section 3.1 and 3.1.3), without any significant contribution from phase transformation-related effects. This is representative of the actual service of turbine parts, which are usually designed to operate the TBC within "safe" conditions to achieve a long lifetime.

More specifically, it is found that with both low- and high-porosity top coats, a TGO thickness threshold of approximately 5 µm exists (Fig. 7A), which is in excellent accordance with a previous study [22]. Below that threshold, TGO thickness increases linearly, with the correspondingly slow progress of delamination cracks. Above the threshold, the TGO grows rapidly in thickness, up to a maximum of ≈10 µm towards the end of the test. Ref. [22] also reported near-zero residual lifetime of the TBC system when the TGO thickness was >9 µm.

Pillar splitting tests further reveal that, if the TGO layer grows dense and compact below the threshold, its fracture toughness even increases, possibly aided by the toughening effect of the yttrium-rich inclusions. As oxidation progresses, stresses within the TGO and at its interface with the bond coat become ever larger, as revealed by a finite element study [59]. Measurement of TGO stress was not carried out in this work, since measuring stresses on a polished cross-section might lead to unreliable results. The sectioning process would indeed involve stress relaxation that should be properly taken into account. Such an activity goes beyond the scope of this work and, at the same time, literature papers (such as the previously cited one) have already examined the stress evolution within the TGO. At the threshold thickness, stresses within the TGO overcome its toughness. It must indeed be reminded that the present toughness values are independent of residual stresses, which are fully relieved within a machined pillar. Once significant crack formation begins, the loss in TGO compactness allows direct access of oxygen to the MCrAlY surface. Increased oxidation rate results in faster growth of the scale and simultaneously depletes the bond coat of its β-NiAl reservoir. Most of the bond coating indeed becomes depleted of β-NiAl soon after the threshold is exceeded (after 634 cycles – Section 3.1.2 and Fig. 3E, F) and the β-NiAl phase itself is visibly altered in its structure and morphology through the formation of lamellar martensite (Fig. 4). Almost no surviving β-phase after 714 cycles confirms that the actual lifetime of the TBC system has practically been exhausted at that point. Aluminium diffusion becomes insufficient to sustain the growth of a purely Al-based scale; therefore, other oxides are formed, which are based on Ni, Co and, possibly, some Cr, as shown by the EDX spectra in Fig. 6C, D (see Section 3.1.2). The phenomenon has been largely

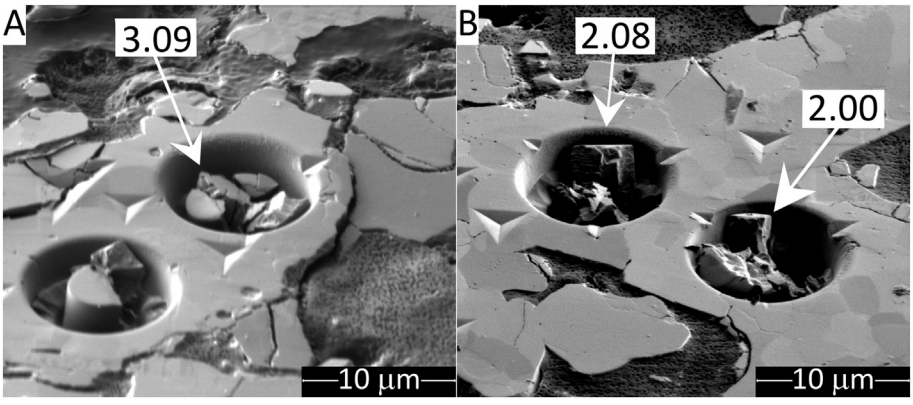

Fig. 18. SEM micrographs showing details of pillars in coarse-grained (A) and fine-grained (B) regions after splitting. Numbers next to each pillar represent the fracture toughness obtained as a result of splitting (in MPa·√m).

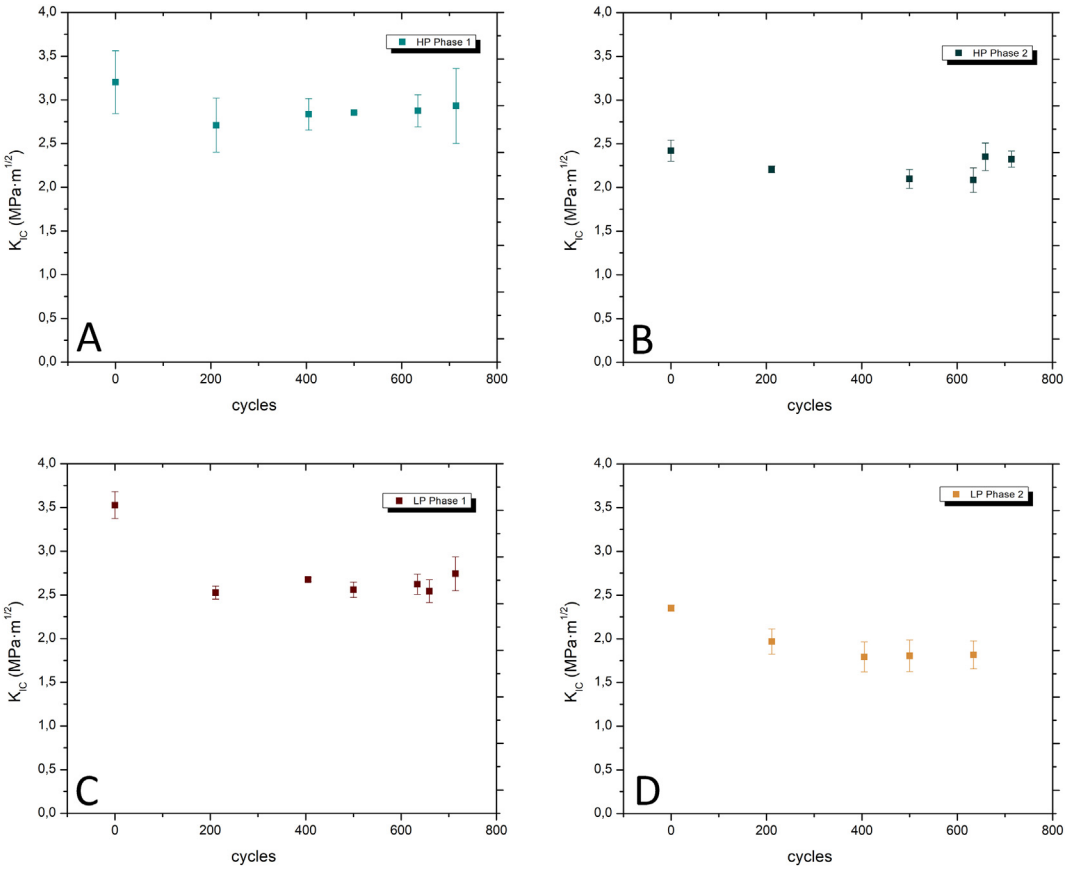

Fig. 19. Fracture toughness values of regions 1 and 2, for both low- and high-porosity YSZ coatings, as a function of the number of TCF cycles – A: HP, region 1; B: HP, region 2; C: LP – region 1; D: LP – region 2.

documented in the literature, for instance in [60]. These oxides grow faster than alumina, additionally contributing to the rapid increase in TGO thickness. Moreover, their presence within the TGO is probably the reason why its fracture toughness, again measured from pillar splitting tests, decreases after the threshold and especially after ≈600 cycles.

It is therefore concluded that, in accordance with [21,22], a change in the mechanism of crack formation occurs at the critical thickness threshold. Below the threshold, the maximum fracture toughness values of the TGO (2.5–3.5 MPa·√m after ≈400 cycles, Fig. 7B) are comparable to or even higher than the corresponding toughness of YSZ (Fig. 19); therefore, short cracks open preferentially in the YSZ layer (which already contains numerous defects) rather than in the TGO, as noted in Section 3.1. Above the threshold, cracks develop in the TGO and continue to do so even though their formation relieves part of the TGO stress [61]. TGO toughness, indeed, correspondingly decreases. Since, as postulated in [59], the cracked TGO transfers stress to the YSZ layer, the result is that cracks starting in the TGO connect to each other by propagating across the top coat, merging into the long delamination cracks noted in Section 3.1, consistent with [17].

Together with the above evolution of the TGO, the top coat undergoes progressive sintering as described in Section 3.1.3. Although this does not look like the primary cause of failure, it can accelerate the progression of delamination cracks discussed above.

Much has been said on the macroscopic progression of sintering (e.g.: [12,57,62–65]) and its negative effects on thermal fatigue life [66,67]; hence, the present paper does not aim to analyse again those known phenomena, which are here simply summarized, based on the cited references. At the macro-scale, the overall elastic modulus of the top coat increases as porosity is reduced due to sintering (as seen in Fig. 2 as well), until the overly stiffened ceramic develops transverse cracks during cooling. This was seen to occur after >600 cycles in the present TCF tests (Section 3.1 and Fig. 1), which leads to a slight increase in overall pore volume (Fig. 2). At that point, the macro-scale elastic modulus starts decreasing. As long as the elastic modulus keeps increasing, the stress state in the vicinity of the TGO becomes more severe and contributes to the opening of the delamination cracks [61]. Transverse cracks interfere with the stress state around the delamination cracks themselves [66], thus contributing further to accelerated delamination in spite of a reduction in macro-scale modulus.

However, the present analyses also revealed changes over a smaller length scale. High-speed nanoindentation tests (Fig. 15) particularly highlighted an apparent reduction of the average hardness and elastic modulus values of both coarse-grained regions (the third "mechanical phase" identified in Section 3.2) and fine-grained regions (the second "mechanical phase") after ≈600 TCF cycles, in both high- and low-porosity coatings. This is most likely the manifestation of the small-scale microstructural changes described in Section 3.1.3.

The hardness and elastic modulus ($H_{IT} \approx 20$ GPa and $E_{IT} \approx 245$ GPa) of the third "mechanical phase", corresponding to coarse-grained equiaxed regions (Section 3.2), initially match reasonably well with the hardness and modulus of single-crystal YSZ averaged over different orientations, as inferable from [68]. Their decrease corresponds to the appearance of distributed, fine porosity in these equiaxed regions, as shown in Fig. 9C, D. The micrographs clarify that such porosity results from the interplay between thermal shock during forced cooling, which continuously opens up new defects, and sintering at high-temperature, which tends to close those defects. The literature [13]

also corroborates this interpretation. Those pores are so widely distributed (Fig. 9C) that they can affect the response of the probed material even with a load as small as 3 mN.

The second "mechanical phase" corresponds to the columnar fine-grained regions: their lower hardness and elastic modulus reflect the poorer mechanical strength of the numerous grain boundaries, consistent with the pillar splitting results discussed previously. The rearrangement of columnar grains into fine equiaxed ones (Section 3.1.3, also compare Fig. 9B to Fig. 9D) causes the specific grain boundary surface to increase even further, with a corresponding decrease in mechanical properties.

It is therefore inferred that sintering and grain restructuring accelerate the top coat failure not only because of the known alteration of the "macroscopic" mechanical response but also because of weakening at the micro-scale.

Those effects were not inferable from fracture toughness measurements (Section 3.3.1). Since the responses of both columnar grains and fine equiaxed grains enter the low-toughness "region 2" data (both types of regions involving numerous, weak grain boundaries), the effect of grain restructuring is probably not so clearly perceivable. The effects of the fine intergranular porosity were also missed because pores could not be included in pillars. Splitting load values measured on pillars that include voids would have indeed been highly scattered and, therefore, statistically unmanageable. It would have been too time-consuming to perform enough pillar-splitting tests to allow for the same type of deconvolution approach employed e.g. for high-speed nanoindentation tests.

It should also be noted that actual service conditions might be more complex than they are in a thermal cycling fatigue test: tensile stresses acting on rotating parts (blades), in particular, can interfere with top coat sintering and delamination cracking. On the one hand, sintering is somewhat hindered or, at least, delayed by tensile stresses [69]. This is especially true for macro-scale cracks and pores [70,71], whereas short-range sintering phenomena such as the closure of microcracks, that mainly depend on surface diffusion, are rather independent of the applied stress [70,71]. Stiffening can therefore occur in spite of such hindrance [70]. Moreover, since short-range sintering is probably the main factor behind the observed formation of distributed fine porosity, the above considerations on its role in favouring delamination crack progression are relevant to actual service conditions. On the other hand, creep of the superalloy substrate under tensile loading worsens the stress state in the YSZ/TGO interface region [72], so that cracks can propagate even during the high-temperature stage and not only during the rapid cooling stages. This might accelerate damage progression, but it does not affect the fundamental damage mechanisms described in this section.

The present results therefore have numerous, practical implications from an engineering point of view. The availability of accurate data on the mechanical properties of TBC constituents as a function of the number of thermal cycles (including the "intrinsic" elastic modulus of the top coat and the toughness of both the top and bond coat) can improve the accuracy of finite element simulations of stress accumulation and damage progression in these systems (e.g. [59,73,74]). Through these simulations, microstructural features such as bond coat roughness or top coat porosity can be designed in order to delay crack growth under various service conditions.

The development of bond coat compositions forming a tougher TGO layer can also be facilitated by the novel availability of a method for directly measuring such toughness. Modifications to standard MCrAlY compositions have been investigated for a long time. Reactive elements (such as Hf) have been introduced to contribute further toughening "pegs" within the alumina-based scale, in addition to those developed by yttrium itself as seen in Fig. 6A, B and in Section 3.1.2 [75]. Alternatively, noble metals such as Re can (among other effects) form tiny metal inclusions within the TGO, again resulting in a toughening effect [75,76]. Up until now, however, actual improvements to TGO toughness could not be quantified but only inferred indirectly from the results of TCF tests. Likewise, much research is ongoing to develop new top coat materials and deposition methods exhibiting either improved toughness, better high temperature stability, or lower thermal conductivity [77,78]. The present observation of previously undocumented phenomena, such as the loss of YSZ toughness upon immediate exposure to thermal cycling conditions or its further mechanical impairment due to distributed porosity in later TCF stages, can give new direction to such development.

5. Conclusions

The present work provided new insight into the progression of thermal cycling damage in thermal barrier coating (TBC) systems, through a characterization of the nano-mechanical properties of plasma-sprayed YSZ top coats and of the underlying thermally grown oxide (TGO) layers. Damage evolution was also observed by scanning electron microscopy.

The following conclusions can be drawn:

1) The existence of a critical TGO thickness of ≈5 μm, as postulated by previous research, is confirmed experimentally, and correlated to a measurable trend of micro-scale fracture toughness.
   Until this threshold, the TGO is solely based on aluminium oxide with yttrium-rich inclusions. It grows slowly and generally remains dense and compact (except for some prominent asperities), as its fracture toughness grows up to maxima of 2.5–3.5 MPa·√m.
2) The as-deposited YSZ top coat consists almost exclusively of the non-transformable tetragonal phase (t'), arranged in both coarse equiaxed grains (mostly within unmelted or re-solidified particles) and fine columnar grains (within impact-quenched, molten lamellae). The hardness ($H_{IT} \approx 20$ GPa), elastic modulus ($E_{IT} \approx 245$ GPa) and fracture toughness ($K_{IC} \approx 3.5$ MPa·√m) of coarse-grained regions correspond to the properties of bulk t'-YSZ, whilst fine-grained regions possess somewhat lower mechanical properties, probably because grain boundaries are a source of weakness.
   In the early stages of the thermal cycling fatigue (TCF) test, some reorganization of the defect structure within the t' lattice (probably due to oxygen uptake from the atmosphere) is accompanied by a slight reduction in the fracture toughness of both coarse- and fine-grained regions. As a result, short delamination cracks form within the YSZ top coat, because its fracture toughness ($K_{IC} \leq 2.5$ MPa·√m) becomes comparable to or even slightly lower than that of the dense TGO. In any case, delamination damage in this short-crack regime progresses slowly.
3) After a sufficient number of cycles, the TGO reaches the critical thickness threshold and starts cracking severely, probably because it has accumulated excessively high stresses. The growth rate of the damaged TGO increases remarkably, accelerating the depletion of the β-NiAl phase in the underlying bond coat. Consequently, (Ni, Co)-based oxides appear, which cause a decrease in the fracture toughness of the TGO below 2.5 MPa·√m.
   Decreased TGO toughness means that cracks continue to propagate even after stresses have been partly relieved. The progression of delamination damage, therefore, accelerates remarkably and the TGO becomes its main source.
4) Towards the end of the TCF test, damage initiated in the TGO readily propagates across the YSZ layer and develops into long delamination cracks, because the mechanical strength of YSZ is impaired, as testified by the reduction in hardness and elastic modulus.
   Fine columnar grains in the YSZ layer are indeed re-arranged into even finer equiaxed grains, and abundant intergranular porosity is developed through the interplay of the crack opening (by thermal shock) and crack healing (by sintering). Both intergranular pores and grain boundaries are sources of weakness. No effect on micro-scale fracture toughness is noted, probably because toughness was always measured in pore-free regions.

Data availability

The raw/processed data required to reproduce these findings cannot be shared at this time as the data also forms part of an ongoing study.

CRediT authorship contribution statement

Giovanni Bolelli: Conceptualization, Investigation, Formal analysis, Writing - original draft. **Maria Grazia Righi:** Investigation. **Muhammad Zeeshan Mughal:** Investigation, Formal analysis, Writing - original draft. **Riccardo Moscatelli:** Investigation. **Omar Ligabue:** Investigation. **Nelso Antolotti:** Writing - review & editing, Supervision. **Marco Sebastiani:** Conceptualization, Formal analysis, Writing - original draft. **Luca Lusvarghi:** Conceptualization, Writing - review & editing, Supervision. **Edoardo Bemporad:** Conceptualization, Writing - review & editing, Supervision.

Acknowledgements

FIB pillar fabrication and nanoindentation experiments were performed at the interdepartmental laboratory of electron microscopy (LIME) of "Roma TRE" University, Rome, Italy.

Many thanks to Turbocoating S.p.A. R&D Dep.

References

[1] S. Bose, High Temperature Coatings, Butterworth-Heinemann, Oxford, UK, 2007.
[2] R. Darolia, Thermal barrier coatings technology: critical review, progress update, remaining challenges and prospects, Int. Mater. Rev. 58 (2013) 315–348.
[3] J.T. DeMasi-Marcin, D.K. Gupta, Protective coatings in the gas turbine engine, Surf. Coat. Technol. 68 (1994) 1–9.
[4] N.P. Padture, Thermal barrier coatings for gas-turbine engine applications, Science 296 (2002) 280–284.
[5] J. Smialek, R. Miller, Revisiting the birth of 7YSZ thermal barrier coatings: Stephan Stecura, Coatings 8 (2018) 255.
[6] J.R. Brandon, R. Taylor, Phase stability of zirconia-based thermal barrier coatings: part 1. Zirconia Yttria alloys, Surf. Coat. Technol. 46 (1991) 75–90.
[7] C. Mercer, J.R. Williams, D.R. Clarke, A.G. Evans, On a ferroelastic mechanism governing the toughness of metastable tetragonal-prime (t′) yttria-stabilized zirconia, Proc. R. Soc. A Math. Phys. Eng. Sci. 463 (2007) 1393–1408.
[8] R. Ragupathy, R.K. Mishra, R.D. Misal, Life estimation of TBC on an aero gas turbine combustor: a finite element approach, ASME 2011 Turbo Expo Turbine Tech. Conf. Expo. Vol. 5 Heat Transf. Parts A-B 2011, pp. 2037–2043.
[9] W. Beele, G. Marijnissen, A. Van Lieshout, The evolution of thermal barrier coatings - status and upcoming solutions for today's key issues, Surf. Coat.Technol. 120–121 (1999) 61–67.
[10] R.G. Wellman, J.R. Nicholls, A review of the erosion of thermal barrier coatings, J. Phys. D. Appl. Phys. 40 (2007) R293–R305.
[11] D.R. Clarke, C.G. Levi, Materials design for the next generation thermal barrier coatings, Annu. Rev. Mater. Res. 33 (2003) 383–417.
[12] J. Ilavsky, G.G. Long, A.J. Allen, C.C. Berndt, Evolution of the void structure in plasma-sprayed YSZ deposits during heating, Mater. Sci. Eng. A 272 (1999) 215–221.
[13] F. Tang, J.M. Schoenung, Evolution of Young's modulus of air plasma sprayed yttria-stabilized zirconia in thermally cycled thermal barrier coatings, Scr. Mater. 54 (2006) 1587–1592.
[14] J.A. Krogstad, Y. Gao, J. Bai, J. Wang, D.M. Lipkin, C.G. Levi, In situ diffraction study of the high-temperature decomposition of t'-zirconia, J. Am. Ceram. Soc. 98 (2015) 247–254.
[15] J.A. Krogstad, R.M. Leckie, S. Krämer, J.M. Cairney, D.M. Lipkin, C.A. Johnson, C.G. Levi, Phase evolution upon aging of air plasma sprayed t'-zirconia coatings: II-microstructure evolution, J. Am. Ceram. Soc. 96 (2013) 299–307.
[16] D.M. Lipkin, J.A. Krogstad, Y. Gao, C.A. Johnson, W.A. Nelson, C.G. Levi, Phase evolution upon aging of air-plasma sprayed t'-zirconia coatings: I - synchrotron X-ray diffraction, J. Am. Ceram. Soc. 96 (2013) 290–298.
[17] J.T. DeMasi-Marcin, K.D. Sheffler, S. Bose, Mechanisms of degradation and failure in a plasma-deposited thermal barrier coating, J. Eng. Gas Turbines Power 112 (1990) 521–526.
[18] S.T. Kyaw, I.A. Jones, T.H. Hyde, Simulation of failure of air plasma sprayed thermal barrier coating due to interfacial and bulk cracks using surface-based cohesive interaction and extended finite element method, J. Strain Anal. Eng. Des. 51 (2016) 132–143.
[19] K.P. Jonnalagadda, R. Eriksson, K. Yuan, X.-H. Li, X. Ji, Y. Yu, R.L. Peng, A study of damage evolution in high purity nano TBCs during thermal cycling: a fracture mechanics based modelling approach, J. Eur. Ceram. Soc. 37 (2017) 2889–2899.
[20] W. Xie, E. Jordan, M. Gell, Stress and cracking behavior of plasma sprayed thermal barrier coatings using an advanced constitutive model, Mater. Sci. Eng. A 419 (2006) 50–58.
[21] J. Yang, L. Wang, D. Li, X. Zhong, H. Zhao, S. Tao, Stress analysis and failure mechanisms of plasma-sprayed thermal barrier coatings, J. Therm. Spray Technol. 26 (2017) 890–901.
[22] C.J. Li, H. Dong, H. Ding, G.J. Yang, C.X. Li, The correlation of the TBC lifetimes in burner cycling test with thermal gradient and furnace isothermal cycling test by TGO effects, J. Therm. Spray Technol. 26 (2017) 378–387.
[23] M. Sebastiani, R. Moscatelli, F. Ridi, P. Baglioni, F. Carassiti, High-resolution high-speed nanoindentation mapping of cement pastes: unravelling the effect of microstructure on the mechanical properties of hydrated phases, Mater. Des. 97 (2016) 372–380.
[24] J.J. Roa, P. Sudharshan Phani, W.C. Oliver, L. Llanes, Mapping of mechanical properties at microstructural length scale in WC-Co cemented carbides: assessment of hardness and elastic modulus by means of high speed massive nanoindentation and statistical analysis, Int. J. Refract. Met. Hard Mater. 75 (2018) 211–217.
[25] E.P. Koumoulos, S.A.M. Tofail, C. Silien, D. De Felicis, R. Moscatelli, D.A. Dragatogiannis, E. Bemporad, M. Sebastiani, C.A. Charitidis, Metrology and nanomechanical tests for nano-manufacturing and nano-bio interface: challenges & future perspectives, Mater. Des. 137 (2018) 446–462.
[26] W. Oliver, G. Pharr, An improved technique for determining hardness and elastic modulus using load and displacement-sensing indentation systems, J. Mater. Res. 7 (1992) 1564–1583.
[27] W.C. Oliver, G.M. Pharr, Measurement of hardness and elastic modulus by instrumented indentation: advances in understanding and refinements to methodology, J. Mater. Res. 19 (2004) 3–20.
[28] F.J. Ulm, Chemomechanics of concrete at finer scales, Mater. Struct. Constr. 36 (2003) 426–438.
[29] M. Vandamme, F.J. Ulm, P. Fonollosa, Nanogranular packing of C-S-H at substochiometric conditions, Cem. Concr. Res. 40 (2010) 14–26.
[30] M. Sebastiani, K.E. Johanns, E.G. Herbert, F. Carassiti, G.M. Pharr, A novel pillar indentation splitting test for measuring fracture toughness of thin ceramic coatings, Philos. Mag. 95 (2015) 1928–1944.
[31] M. Sebastiani, K.E. Johanns, E.G. Herbert, G.M. Pharr, Measurement of fracture toughness by nanoindentation methods: recent advances and future challenges, Curr. Opin. Solid State Mater. Sci. 19 (2015) 324–333.
[32] M. Ghidelli, M. Sebastiani, K.E. Johanns, G.M. Pharr, Effects of indenter angle on micro-scale fracture toughness measurement by pillar splitting, J. Am. Ceram. Soc. 100 (2017) 5731–5738.
[33] E. Salvati, T. Sui, A.J.G. Lunt, A.M. Korsunsky, The effect of eigenstrain induced by ion beam damage on the apparent strain relief in FIB-DIC residual stress evaluation, Mater. Des. 92 (2016) 649–658.
[34] J.P. Best, J. Zechner, J.M. Wheeler, R. Schoeppner, M. Morstein, J. Michler, Small-scale fracture toughness of ceramic thin films: the effects of specimen geometry, ion beam notching and high temperature on chromium nitride toughness evaluation, Philos. Mag. 96 (2016) 3552–3569.
[35] M. Renzelli, M.Z. Mughal, M. Sebastiani, E. Bemporad, Design, fabrication and characterization of multilayer Cr-CrN thin coatings with tailored residual stress profiles, Mater. Des. 112 (2016) 162–171.
[36] M.Z. Mughal, R. Moscatelli, H.Y. Amanieu, M. Sebastiani, Effect of lithiation on microscale fracture toughness of $Li_xMn_2O_4$ cathode, Scr. Mater. 116 (2016) 62–66.
[37] M.Z. Mughal, H.-Y. Amanieu, R. Moscatelli, M. Sebastiani, A comparison of microscale techniques for determining fracture toughness of $LiMn_2O_4$ particles, Materials 10 (2017) 403.
[38] I.R. Gibson, J.T.S. Irvine, Qualitative X-ray diffraction analysis of metastable tetragonal (t′) zirconia, J. Am. Ceram. Soc. 84 (2001) 615–618.
[39] J.R. Kelly, I. Denry, Stabilized zirconia as a structural ceramic: an overview, Dent. Mater. 24 (2008) 289–298.
[40] F. Cernuschi, S. Capelli, P. Bison, S. Marinetti, L. Lorenzoni, E. Campagnoli, C. Giolli, Non-destructive thermographic monitoring of crack evolution of thermal barrier coating coupons during cyclic oxidation aging, Acta Mater. 59 (2011) 6351–6361.
[41] J. Toscano, R. Vaβen, A. Gil, M. Subanovic, D. Naumenko, L. Singheiser, W.J. Quadakkers, Parameters affecting TGO growth and adherence on MCrAlY-bond coats for TBC's, Surf. Coat. Technol. 201 (2006) 3906–3910.
[42] W. Beele, N. Czech, W.J. Quadakkers, W. Stamm, Long-term oxidation tests on a re-containing MCrAlY coating, Surf. Coat. Technol. 94–95 (1997) 41–45.
[43] E.A.G. Shillington, D.R. Clarke, Spalling failure of a thermal barrier coating associated with aluminum depletion in the bond-coat, Acta Mater. 47 (1999) 1297–1305.
[44] P. Krukovsky, V. Kolarik, K. Tadlya, A. Rybnikov, I. Kryukov, N. Mojaiskaya, M. Juez-Lorenzo, Lifetime prediction for MCrAlY coatings by means of inverse problem solution (IPS), Surf. Coat. Technol. 177–178 (2004) 32–36.
[45] Y. Itoh, M. Tamura, Reaction diffusion behaviors for interface between Ni-based super alloys and vacuum plasma sprayed MCrAlY coatings, Trans. ASME 121 (1999) 476–483.
[46] R.A. Page, G.R. Leverant, Inhibition of interdiffusion from MCrAlY overlay coatings by application of a Ni-Re interlayer, Proc. ASME 1998 Int. Gas Turbine Aeroengine Congr. Exhib. Vol. 5 Manuf. Mater. Metall. Ceram. Struct. Dyn. Control. Diagnostics Instrumentation; Educ, 1998 , (p. V005T12A003).
[47] M.W. Chen, R.T. Ott, T.C. Hufnagel, P.K. Wright, K.J. Hemker, Microstructural evolution of platinum modified nickel aluminide bond coat during thermal cycling, Surf. Coat. Technol. 163–164 (2003) 25–30.
[48] B.G. Mendis, B. Tryon, T.M. Pollock, K.J. Hemker, Microstructural observations of as-prepared and thermal cycled NiCoCrAlY bond coats, Surf. Coat. Technol. 201 (2006) 3918–3925.
[49] M.W. Chen, K.J.T. Livi, K.J. Hemker, P.K. Wright, Microstructural characterization of a platinum-modified diffusion aluminide bond coat for thermal barrier coatings, Metall. Mater. Trans. A 34 (2003) 2289–2299.
[50] I.M. Robertson, C.M. Wayman, Tweed microstructures I. Characterization in β-NiAl, Philos. Mag. A 48 (1983) 421–442.
[51] B.G. Mendis, K.J. Hemker, Evolution of the premartensitic state in the NiAl phase of a NiCoCrAlY bond coat during thermal cycling, Philos. Mag. 87 (2007) 4229–4251.

[52] L. Bianchi, A. Denoirjean, F. Blein, P. Fauchais, Microstructural investigation of plasma-sprayed ceramic splats, Thin Solid Films 299 (1997) 125–135.
[53] V. Lughi, D.R. Clarke, Transformation of electron-beam physical vapor-deposited 8 wt% yttria-stabilized zirconia thermal barrier coatings, J. Am. Ceram. Soc. 88 (2005) 2552–2558.
[54] S. Nath, I. Manna, J.D. Majumdar, Nanomechanical behavior of yttria stabilized zirconia (YSZ) based thermal barrier coating, Ceram. Int. 41 (2015) 5247–5256.
[55] W.G. Mao, J.M. Luo, C.Y. Dai, Y.G. Shen, Effect of heat treatment on deformation and mechanical properties of 8 mol% yttria-stabilized zirconia by Berkovich nanoindentation, Appl. Surf. Sci. 338 (2015) 92–98.
[56] G.M. Ingo, Origin of darkening in 8 wt% yttria—zirconia plasma-sprayed thermal barrier coatings, J. Am. Ceram. Soc. 74 (1991) 381–386.
[57] P. Strunz, G. Schumacher, R. Vassen, A. Wiedenmann, In situ SANS study of pore microstructure in YSZ thermal barrier coatings, Acta Mater. 52 (2004) 3305–3312.
[58] V. Lughi, D.R. Clarke, High temperature aging of YSZ coatings and subsequent transformation at low temperature, Surf. Coat. Technol. 200 (2005) 1287–1291.
[59] K. Slámečka, P. Skalka, J. Pokluda, L. Čelko, Finite element simulation of stresses in a plasma-sprayed thermal barrier coating with an irregular top-coat/bond-coat interface, Surf. Coat. Technol. 304 (2016) 574–583.
[60] W.R. Chen, R. Archer, X. Huang, B.R. Marple, TGO growth and crack propagation in a thermal barrier coating, J. Therm. Spray Technol. 17 (2008) 858–864.
[61] J.P. Singh, B.G. Nair, D.P. Renusch, M.P. Sutaria, M.H. Grimsditch, Damage evolution and stress analysis in zirconia thermal barrier coatings during cyclic and isothermal oxidation, J. Am. Ceram. Soc. 84 (2004) 2385–2393.
[62] Q. Chen, W.G. Mao, Y.C. Zhou, C. Lu, Effect of Young's modulus evolution on residual stress measurement of thermal barrier coatings by X-ray diffraction, Appl. Surf. Sci. 256 (2010) 7311–7315.
[63] M.A. Helminiak, N.M. Yanar, F.S. Pettit, T.A. Taylor, G.H. Meier, Factors affecting the microstructural stability and durability of thermal barrier coatings fabricated by air plasma spraying, Mater. Corros. 63 (2012) 929–939.
[64] S. Paul, A. Cipitria, S.A. Tsipas, T.W. Clyne, Sintering characteristics of plasma sprayed zirconia coatings containing different stabilisers, Surf. Coat. Technol. 203 (2009) 1069–1074.
[65] P.A. Langjahr, R. Oberacker, M.J. Hoffmann, Long-term behavior and application limits of plasma-sprayed zirconia thermal barrier coatings, J. Am. Ceram. Soc. 84 (2004) 1301–1308.
[66] H. Dong, J.-T. Yao, X. Li, Y. Zhou, Y.-B. Li, The sintering behavior of plasma-sprayed YSZ coating over the delamination crack in low temperature environment, Ceram. Int. 44 (2018) 3326–3332.
[67] B. Cheng, Y.M. Zhang, N. Yang, M. Zhang, L. Chen, G.J. Yang, C.X. Li, C.J. Li, Sintering-induced delamination of thermal barrier coatings by gradient thermal cyclic test, J. Am. Ceram. Soc. 100 (2017) 1820–1830.
[68] M. Fujikane, D. Setoyama, S. Nagao, R. Nowak, S. Yamanaka, Nanoindentation examination of yttria-stabilized zirconia (YSZ) crystal, J. Alloys Compd. 431 (2007) 250–255.
[69] S.A. Tsipas, I.O. Golosnoy, R. Damani, T.W. Clyne, The effect of a high thermal gradient on sintering and stiffening in the top coat of a thermal barrier coating system, J. Therm. Spray Technol. 13 (2004) 370–376.
[70] M. Ahrens, S. Lampenscherf, R. Vaßen, D. Stöver, Sintering and creep processes in plasma-sprayed thermal barrier coatings, J. Therm. Spray Technol. 13 (2004) 432–442.
[71] A. Cipitria, I.O. Golosnoy, T.W. Clyne, A sintering model for plasma-sprayed zirconia thermal barrier coatings. Part II: coatings bonded to a rigid substrate, Acta Mater. 57 (2009) 993–1003.
[72] E.P. Busso, J. Lin, S. Sakurai, M. Nakayama, A mechanistic study of oxidation-induced degradation in a plasma-sprayed thermal barrier coating system. Part I: model formulation, Acta Mater. 49 (2001) 1515–1528.
[73] U. Hermosilla, M.S.A. Karunaratne, I.A. Jones, T.H. Hyde, R.C. Thomson, Modelling the high temperature behaviour of TBCs using sequentially coupled microstructural-mechanical FE analyses, Mater. Sci. Eng. A 513–514 (2009) 302–310.
[74] M. Ranjbar-Far, J. Absi, G. Mariaux, Finite element modeling of the different failure mechanisms of a plasma sprayed thermal barrier coatings system, J. Therm. Spray Technol. 21 (2012) 1234–1244.
[75] A. Feuerstein, J. Knapp, T. Taylor, A. Ashary, A. Bolcavage, N. Hitchman, Technical and economical aspects of current thermal barrier coating systems for gas turbine engines by thermal spray and EBPVD: a review, J. Therm. Spray Technol. 17 (2008) 199–213.
[76] N. Czech, F. Schmitz, W. Stamm, Improvement of MCrAlY coatings by addition of rhenium, Surf. Coat. Technol. 68–69 (1994) 17–21.
[77] E. Bakan, R. Vaßen, Ceramic top coats of plasma-sprayed thermal barrier coatings: materials, processes, and properties, J. Therm. Spray Technol. 26 (2017) 992–1010.
[78] G. Mauer, M.O. Jarligo, D.E. Mack, R. Vaßen, Plasma-sprayed thermal barrier coatings: new materials, processing issues, and solutions, J. Therm. Spray Technol. 22 (2013) 646–658.